

# Dynamics of dark energy in a scalar-vector-torsion theory

Manuel Gonzalez-Espinoza,<sup>1,\*</sup> Giovanni Otalora,<sup>2,†</sup> Yoelsy Leyva,<sup>2,‡</sup> and Joel Saavedra<sup>3,§</sup>

<sup>1</sup>*Departamento de Matemática, Física y Computación,  
Facultad de Ciencias Naturales y Exactas, Universidad de Playa Ancha,  
Subida Leopoldo Carvallo 270, Valparaíso, Chile.*

<sup>2</sup>*Departamento de Física, Facultad de Ciencias, Universidad de Tarapacá, Casilla 7-D, Arica, Chile*

<sup>3</sup>*Instituto de Física, Pontificia Universidad Católica de Valparaíso, Casilla 4950, Valparaíso, Chile*

(Dated: July 11, 2023)

We study the cosmological dynamics of dark energy in a scalar-vector-torsion theory. The vector field is described by the cosmic triad and the scalar field is of the quintessence type with non-minimal coupling to gravity. The coupling to gravity is introduced through the interaction between the scalar field and torsion, where torsion is defined in the context of teleparallel gravity. We derive the full set of field equations for the Friedmann–Lemaître–Robertson–Walker space-time background and obtain the associated autonomous system. We obtain the critical points and their stability conditions, along with the cosmological properties of them. Thus, we show that the thermal history of the universe is successfully reproduced. Furthermore, new scaling solutions in which the scalar and vector field densities scale in the same way as the radiation and matter background fluids have been found. Finally, we also show that there exist new attractor fixed points whose nature is mainly vectorial, and which can explain the current accelerated expansion and therefore the dark energy-domination.

PACS numbers: 04.50.Kd, 98.80.-k, 95.36.+x

## I. INTRODUCTION

Currently, one of the biggest puzzles in cosmology is called dark energy [1, 2]. It is believed that dark energy is responsible for the late-time acceleration of the Universe and constitutes 68% of the total energy density, along with the other 32% associated to dark matter [3]. The simplest explanation is related to the  $\Lambda$ CDM model, but it is plagued with theoretical problems, such as the severe fine tuning problem related to its energy scale, the so-called cosmological constant problem [4–6]. Furthermore, recently some tensions with increasing statistical significance have been found when comparing the  $\Lambda$ CDM model predictions for cosmological observables by using the cosmic microwave background (CMB) data and the values obtained from independent local measurements [7–10]. For instance, the value for the Hubble constant today  $H_0$  estimated from Planck data using the  $\Lambda$ CDM model is  $4.0\sigma$  to  $6.3\sigma$  below current local measurements [11], and also the clustering amplitude  $\sigma_8$  value deduced from Planck data by using the  $\Lambda$ CDM model is above that obtained from low-redshift observations [10, 12–14].

As a consequence of these latest findings, the interest in modified gravity models to explain dark energy has increased [15–17]. On the one hand, the torsional modified gravity theories are constructed as extensions of the so-called Teleparallel Equivalent of General Relativity, or just Teleparallel Gravity (TG) [18–30], whose best-known example is  $f(T)$  gravity [31–33]. For instance,

from the perspective of effective field theories (EFT), in Ref. [34] the authors have shown that some models of  $f(T)$  gravity can efficiently fit observations solving both  $H_0$  and  $\sigma_8$  tensions simultaneously. Also, the generalized scalar-torsion  $f(T, \phi)$  gravity theories have been studied [35, 36]. These include a wide family of theories such as  $f(T)$  gravity plus scalar field [37–41], nonminimally coupled scalar-torsion theories [42–51], and their extensions for a nonlinear coupling to torsion [36, 52–54]. Notice that scalar fields are very common in high energy physics and cosmology [55]. Additionally, a nonminimal coupling to gravity can arise naturally either due to quantum corrections to the scalar potential [56], or due to renormalizability requirements [57–59]. Furthermore, these  $f(T, \phi)$  gravity theories have shown a rich structure by explaining the dynamics of dark energy [49, 52, 54, 60–62] and inflation [36, 53, 63] (see also [64] and references therein).

In addition to scalar field models, we also have vector field models to explain the current accelerated expansion of the universe. For instance, in the context of generalized Proca theories, a massive vector field breaking the  $U(1)$  gauge symmetry is introduced and its time-dependent component has been shown to provide us with an asymptotic de Sitter attractor [65–68]. However, if the field is canonical and minimally coupled, its motion equation becomes trivial and then it cannot be a source of dark energy [69]. Let us note that these latter vector theories belong to the class of time-like vector models. On the other hand, space-like vectors have also been considered to model inflation and dark energy [69–73]. Although, space-like models are typically known to generate a highly anisotropic universe this issue can be solved in some special cases. For instance, one way is by assuming a large number of randomly oriented vectors fields that on the average yields an isotropic background cosmology

\* manuel.gonzalez@upla.cl

† giovanni.otalora@academicos.uta.cl

‡ yoelsy.leyva@academicos.uta.cl

§ joel.saavedra@pucv.cl

[74]. Another way is by considering a set of three identical vector fields for each spatial direction, the so-called cosmic triad which is also consistent with the background symmetry [72].

In the present paper, we study the cosmological dynamics of dark energy in a scalar-vector-torsion theory, with the vector representing the cosmic triad and the scalar field is non-minimally coupled to torsion. The plan of this paper is the following: In section II we briefly introduce the basics concepts of TG. In Section III we present the total action of the model and the field equations. In Section IV we obtain the cosmological equations and define the effective dark energy. In Section V we perform a phase-space analysis for the model, obtaining the autonomous system with the corresponding critical points and their stability conditions. In Section VI we corroborate our previous analytical results by numerically solving the field equations. Finally, in Section VIII we summarize the results obtained.

## II. BRIEF INTRODUCTION TO TELEPARALLEL GRAVITY

Teleparallel gravity (TG) is an equivalent description of General Relativity (GR), but based on torsion and not curvature [24, 25, 29, 30]. It is a gauge theory for the translation group [26, 28, 30]. The dynamical variable is the tetrad field which is related to the spacetime metric via

$$g_{\mu\nu} = \eta_{AB} e^A_\mu e^B_\nu, \quad (1)$$

where  $\eta_{AB} = \text{diag}(-1, 1, 1, 1)$  is the Minkowski tangent space metric.

The spin connection of TG is defined as

$$\omega^A_{B\mu} = \Lambda^A_D(x) \partial_\mu \Lambda^D_B(x), \quad (2)$$

where  $\Lambda^A_D(x)$  is a local (point-dependent) Lorentz transformation. For this connection one finds that the curvature tensor vanishes identically

$$R^A_{B\mu\nu} = \partial_\mu \omega^A_{B\nu} - \partial_\nu \omega^A_{B\mu} + \omega^A_{C\mu} \omega^C_{B\nu} - \omega^A_{C\nu} \omega^C_{B\mu} = 0. \quad (3)$$

This is why it is called purely inertial connection or simply flat connection. Moreover, in the presence of gravity this connection gives a non-vanishing torsion tensor

$$T^A_{\mu\nu} = \partial_\mu e^A_\nu - \partial_\nu e^A_\mu + \omega^A_{B\mu} e^B_\nu - \omega^A_{B\nu} e^B_\mu. \quad (4)$$

Using the spin connection one can construct a spacetime-indexed linear connection which is written as

$$\Gamma^\rho_{\nu\mu} = e^A_\rho \partial_\mu e^A_\nu + e^A_\rho \omega^A_{B\mu} e^B_\nu. \quad (5)$$

It is the so-called Weitzenböck connection. By introducing the contortion tensor

$$K^\rho_{\nu\mu} = \frac{1}{2} (T^\rho_{\nu\mu} + T^\rho_{\mu\nu} - T^\rho_{\nu\mu}), \quad (6)$$

and the purely spacetime form of the torsion tensor  $T^\rho_{\mu\nu} = e^A_\rho T^A_{\mu\nu}$  one can verify the following relation

$$\Gamma^\rho_{\nu\mu} = \bar{\Gamma}^\rho_{\nu\mu} + K^\rho_{\nu\mu}, \quad (7)$$

where  $\bar{\Gamma}^\rho_{\nu\mu}$  is the Levi-Civita connection and then

$$T^\rho_{\mu\nu} = \Gamma^\rho_{\nu\mu} - \Gamma^\rho_{\mu\nu}. \quad (8)$$

The action of TG is quadratic in the torsion tensor and it is given by [30]

$$S = -\frac{1}{2\kappa^2} \int d^4x e T, \quad (9)$$

where  $e = \det(e^A_\mu) = \sqrt{-g}$ , and  $T$  is the torsion scalar, which is defined as

$$T = S_\rho^{\mu\nu} T^\rho_{\mu\nu}, \quad (10)$$

with

$$S_\rho^{\mu\nu} = \frac{1}{2} \left( K^{\mu\nu}_\rho + \delta^\mu_\rho T^{\theta\nu}_\theta - \delta^\nu_\rho T^{\theta\mu}_\theta \right), \quad (11)$$

the so-called super-potential.

Interestingly enough, using Eq. (7) one can verify that the torsion scalar  $T$  of the Weitzenböck connection is related to the curvature scalar  $R$  of Levi-Civita connection through

$$T = -R + 2e^{-1} \partial_\mu (e T^{\nu\mu}_\nu), \quad (12)$$

and therefore, TG and GR are equivalent at the level of field equations. Nevertheless, in order to modify gravity we can start either from GR or TG and the resulting theories do not necessarily have to be equivalent. Thus, in the context of TG, one can modify gravity either by adding a non-minimally coupled matter field such as a scalar field [42, 46–49], or considering into the action non-linear terms in the torsion scalar as occurs in  $f(T)$  gravity [31–33, 75]. In this way, these torsion-based modified gravity theories belong to new classes of theories that do not have any curvature-based equivalent. In addition, a rich phenomenology has been found which has given rise to a fair number of articles in cosmology of early and late-time Universe [64].

## III. SCALAR-VECTOR-TORSION THEORY

We start from the action

$$S = - \int d^4x e \left[ \frac{T}{2\kappa^2} + F(\phi)T + \frac{1}{2} \partial_\mu \phi \partial^\mu \phi + V_1(\phi) + \sum_{a=1}^3 \left( \frac{1}{4} \mathcal{F}^a_{\mu\nu} \mathcal{F}^{a\mu\nu} + V_2(A^{a2}) \right) \right] + S_m + S_r, \quad (13)$$

where  $\mathcal{F}^a_{\mu\nu} = \partial_\mu A^a_\nu - \partial_\nu A^a_\mu$  and  $A^{a2} = g^{\mu\nu} A^a_\mu A^a_\nu$ .  $S_m$  is the action of matter.  $S_r$  is the action of radiation.

Varying the action with respect to the tetrad field we obtain the field equations

$$\begin{aligned} & \left( \frac{1}{2\kappa^2} + F(\phi) \right) G_{\mu\nu} + S_{\mu\nu}{}^\rho \partial_\rho F + \\ & \frac{1}{4} g_{\mu\nu} \left[ \frac{1}{2} \partial^\rho \phi \partial_\rho \phi + V_1(\phi) + \sum_{a=1}^3 \left( \frac{1}{4} \mathcal{F}^a{}_{\sigma\rho} \mathcal{F}^{a\sigma\rho} + V_2(A^{a2}) \right) \right] \\ & \frac{1}{4} \partial_\mu \phi \partial_\nu \phi - \frac{1}{4} \sum_{a=1}^3 \left[ \mathcal{F}^a{}_{\rho\mu} \mathcal{F}^{a\rho}{}_\nu + 2A_\mu^a A_\nu^a \frac{dV_2}{dA^{a2}} \right] \\ & = \frac{1}{4} T_{\mu\nu}^{(m)} + \frac{1}{4} T_{\mu\nu}^{(r)}, \end{aligned}$$

where  $G^\mu{}_\nu = e_A{}^\mu G^A{}_\nu$  is the Einstein tensor with [30]

$$\begin{aligned} G_A{}^\mu & \equiv e^{-1} \partial_\nu (e e_A{}^\sigma S_\sigma{}^{\mu\nu}) - e_A{}^\sigma T_{\rho\sigma}^\lambda S_\lambda{}^{\rho\mu} + \\ & e_B{}^\lambda S_\lambda{}^{\rho\mu} \omega^B{}_{A\rho} + \frac{1}{4} e_A{}^\mu T. \end{aligned} \quad (15)$$

Varying with respect to the scalar field  $\phi$  we find the motion equation

$$\nabla_\mu \partial^\mu \phi - F_{,\phi} T - V_{1,\phi} = 0, \quad (16)$$

where  $\nabla_\mu$  is the covariant derivative associated to the Levi-Civita connection. Finally, varying with respect to the cosmic triad  $A_\mu^a$

$$\nabla_\nu \mathcal{F}^{a\nu\mu} - 2 \frac{dV_2}{dA^{a2}} A^{a\mu} = 0. \quad (17)$$

Below we study dynamics of the fields in a cosmological background.

#### IV. COSMOLOGICAL DYNAMICS

In order to study cosmology in the above scalar-vector-torsion theory we choose the background tetrad field

$$e_\mu^A = \text{diag}(1, a, a, a), \quad (18)$$

which corresponds to a flat Friedmann-Robertson-Walker (FRW) universe with metric

$$ds^2 = -dt^2 + a^2 \delta_{ij} dx^i dx^j, \quad (19)$$

where  $a$  is the scale factor which is a function of the cosmic time  $t$ .

We also assume the ansatz

$$A_\mu^a = \delta_\mu^a A(t) a(t). \quad (20)$$

In this way, the three vectors have the same time-dependent length,  $A^{a2} = A(t)^2$ , being that they point in three mutually orthogonal spatial directions [72].

Thus, the modified Friedmann equations are given by

$$\begin{aligned} 6H^2 \left( \frac{1}{2\kappa^2} + F \right) & = \frac{3}{2} (AH + \dot{A})^2 + V_1 + 3V_2 + \frac{\dot{\phi}^2}{2} \\ & + \rho_m + \rho_r, \end{aligned} \quad (21)$$

$$\begin{aligned} -4\dot{H} \left( \frac{1}{2\kappa^2} + F \right) & = 2(AH + \dot{A})^2 + \dot{\phi}^2 + 4H\dot{\phi}F_{,\phi} \\ & + 2A^2 V_{2,A^2} + \rho_m + \frac{4\rho_r}{3}, \end{aligned} \quad (22)$$

along with the motion equation for the fields  $\phi$  and  $A$

$$\ddot{\phi} + 6H^2 F_{,\phi} + 3H\dot{\phi} + V_{1,\phi} = 0, \quad (23)$$

$$\ddot{A} + 2AH^2 + 3\dot{A}H + A\dot{H} + 2AV_{2,A^2} = 0, \quad (24)$$

respectively.

Thus, as in Ref. [76], the Friedmann equations (21) and (22) can be rewritten in their standard form

$$\frac{3}{\kappa^2} H^2 = \rho_{de} + \rho_m + \rho_r, \quad (25)$$

$$-\frac{2}{\kappa^2} \dot{H} = \rho_{de} + p_{de} + \rho_m + \frac{4}{3} \rho_r, \quad (26)$$

where the effective energy and pressure densities are defined as

$$\begin{aligned} \rho_{de} = \rho_v + \rho_s & = \frac{3}{2} (AH + \dot{A})^2 + 3V_2 \\ & + \frac{\dot{\phi}^2}{2} + V_1 - 6H^2 F, \end{aligned} \quad (27)$$

$$\begin{aligned} p_{de} = p_v + p_s & = \frac{1}{2} (AH + \dot{A})^2 - 3V_2 + 2A^2 V_{2,A^2} \\ & + \frac{\dot{\phi}^2}{2} - V_1 + 6H^2 F + 4H\dot{\phi}F_{,\phi} + 4F\dot{H}. \end{aligned} \quad (28)$$

Then, the effective dark energy equation-of-state (EOS) parameter is

$$w_{de} = \frac{p_{de}}{\rho_{de}}. \quad (29)$$

For these definitions of  $\rho_{de}$  and  $p_{de}$  one can verify that they satisfy

$$\dot{\rho}_{de} + 3H(\rho_{de} + p_{de}) = 0. \quad (30)$$

This equation is consistent with the energy conservation law and the fluid evolution equations

$$\dot{\rho}_m + 3H\rho_m = 0, \quad (31)$$

$$\dot{\rho}_r + 4H\rho_r = 0. \quad (32)$$

Also, it is useful to introduce the total EOS parameter as

$$w_{tot} = \frac{p_{de} + p_r}{\rho_{de} + \rho_m + \rho_r}, \quad (33)$$

which is related to the deceleration parameter  $q$  through

$$q = \frac{1}{2}(1 + 3w_{tot}). \quad (34)$$

Then, the acceleration of the Universe occurs for  $q < 0$ , or equivalently for  $w_{tot} < -1/3$ .

Finally, another useful set of cosmological parameters which we can introduce are the so-called standard density parameters

$$\begin{aligned} \Omega_m &\equiv \frac{\kappa^2 \rho_m}{3H^2}, & \Omega_{de} &\equiv \frac{\kappa^2 \rho_{de}}{3H^2} = \Omega_v + \Omega_s, & \Omega_r &\equiv \frac{\kappa^2 \rho_r}{3H^2}, \\ \Omega_v &= \frac{\kappa^2 \rho_v}{3H^2}, & \Omega_s &= \frac{\kappa^2 \rho_s}{3H^2}, \end{aligned} \quad (35)$$

which satisfy the constraint equation

$$\Omega_{de} + \Omega_m + \Omega_r = 1. \quad (36)$$

This latter equation is nothing more than the same energy constraint (25), but written in terms of the energy density parameters.

In terms of these energy density parameters the total equation of state can be also written as

$$w_{tot} = w_v \Omega_v + w_s \Omega_s + \frac{1}{3} \Omega_r, \quad (37)$$

where we have defined

$$w_v = \frac{p_v}{\rho_v}, \quad w_s = \frac{p_s}{\rho_s}, \quad (38)$$

which represent the EOS parameters of the vector and the scalar fields, respectively. Let us remember that for non-relativistic matter one has  $w_m = p_m/\rho_m = 0$ , and for relativistic matter  $w_r = p_r/\rho_r = 1/3$  [77].

In the next section we perform an exhaustive phase space analysis for this dark energy model. Particularly, we obtain the corresponding autonomous system from the set of cosmological equations (25), (26), (31) and (32).

## V. PHASE SPACE ANALYSIS

In order to write the set of the cosmological equations of the model as an autonomous system we introduce the following useful dimensionless variables [76]

$$\begin{aligned} x_1 &= \frac{\kappa \dot{\phi}}{\sqrt{6}H}, & x_2 &= \frac{\kappa \dot{A}}{\sqrt{6}H}, & x_3 &= \frac{\kappa A}{\sqrt{6}}, \\ y_1 &= \frac{\kappa \sqrt{V_1}}{\sqrt{3}H}, & y_2 &= \frac{\kappa \sqrt{V_2}}{\sqrt{3}H}, & u &= -2\kappa^2 F, \\ \lambda_1 &= -\frac{V_{1,\phi}}{\kappa V_1}, & \lambda_2 &= -\frac{V_{2,A^2}}{\kappa^2 V_2}, & \sigma &= -\frac{F_{,\phi}}{\kappa F}, \\ \varrho &= \frac{\kappa \sqrt{\rho_r}}{\sqrt{3}H}, \end{aligned} \quad (39)$$

and the constraint equation

$$\Omega_m + \varrho^2 + u + 3x_2^2 + 3x_3^2 + 6x_2x_3 + 3y_2^2 + x_1^2 + y_1^2 = 1, \quad (40)$$

Therefore, we obtain the dynamical system

$$\begin{aligned} \frac{dx_1}{dN} &= -\frac{f_1(x_1, x_2, x_3, y_1, y_2, u, \varrho)}{2(u-1)}, \\ \frac{dx_2}{dN} &= -\frac{f_2(x_1, x_2, x_3, y_1, y_2, u, \varrho)}{2(u-1)}, \\ \frac{dx_3}{dN} &= x_2, \\ \frac{dy_1}{dN} &= -\frac{y_1 f_3(x_1, x_2, x_3, y_1, y_2, u, \varrho)}{2(u-1)}, \\ \frac{dy_2}{dN} &= -\frac{y_2 f_4(x_1, x_2, x_3, y_1, y_2, u, \varrho)}{2(u-1)}, \\ \frac{du}{dN} &= -\sqrt{6} \sigma_1 u x_1, \\ \frac{d\varrho}{dN} &= -\frac{\varrho f_5(x_1, x_2, x_3, y_1, y_2, u, \varrho)}{2(u-1)}, \\ \frac{d\lambda_1}{dN} &= -\sqrt{6} (\Gamma_1 - 1) \lambda_1^2 x_1, \\ \frac{d\lambda_2}{dN} &= -12 (\Gamma_2 - 1) \lambda_2^2 x_2 x_3, \\ \frac{d\sigma_1}{dN} &= -\sqrt{6} (\Theta_1 - 1) \sigma_1^2 x_1, \end{aligned} \quad (41)$$

where

$$\begin{aligned} f_1 &= 2\sqrt{6} \sigma_1 u x_1^2 + x_1(3u - 36\lambda_2 x_3^2 y_2^2 + 3x_2^2 + 3x_3^2 + 6x_2x_3 \\ &\quad - 3y_1^2 - 9y_2^2 + \varrho^2 - 3) + \sqrt{6}(u-1)(\sigma_1 u - \lambda_1 y_1^2) + 3x_1^3, \\ f_2 &= x_2(u(2\sqrt{6} \sigma_1 x_1 + 3) - 36\lambda_2 x_3^2 y_2^2 + 3x_1^2 + 9x_3^2 - 3y_1^2 \\ &\quad - 9y_2^2 + \varrho^2 - 3) + x_3(2\sqrt{6} \sigma_1 u x_1 - 12\lambda_2 u y_2^2 + u \\ &\quad - 36\lambda_2 x_3^2 y_2^2 + 3x_1^2 + 3x_3^2 + 12\lambda_2 y_2^2 - 3y_1^2 - 9y_2^2 + \varrho^2 - 1) \\ &\quad + 3x_2^3 + 9x_3 x_2^2, \\ f_3 &= u(\sqrt{6} x_1 (\lambda_1 + 2\sigma_1) - 3) - \sqrt{6} \lambda_1 x_1 - 36\lambda_2 x_3^2 y_2^2 + 3x_1^2 \\ &\quad + 3x_2^2 + 3x_3^2 + 6x_2x_3 - 3y_1^2 - 9y_2^2 + \varrho^2 + 3, \\ f_4 &= u(12\lambda_2 x_2 x_3 + 2\sqrt{6} \sigma_1 x_1 - 3) - 12\lambda_2 x_2 x_3 - 36\lambda_2 x_3^2 y_2^2 \\ &\quad + 3x_1^2 + 3x_2^2 + 3x_3^2 + 6x_2x_3 - 3y_1^2 - 9y_2^2 + \varrho^2 + 3, \\ f_5 &= 2\sqrt{6} \sigma_1 u x_1 + u - 36\lambda_2 x_3^2 y_2^2 + 3x_1^2 + 3x_2^2 + 3x_3^2 \\ &\quad + 6x_2x_3 - 3y_1^2 - 9y_2^2 + \varrho^2 - 1. \end{aligned} \quad (42)$$

Using the above set of phase space variables we can also write

$$\begin{aligned} \Omega_{de} &= u + x_1^2 + 3x_2^2 + 3x_3^2 + 6x_2x_3 + y_1^2 + 3y_2^2, \\ \Omega_m &= -u - x_1^2 - 3x_2^2 - 3x_3^2 - 6x_2x_3 - y_1^2 - 3y_2^2 - \varrho^2 + 1. \end{aligned} \quad (43)$$

Similarly, the equation of state of dark energy  $w_{de} =$

TABLE I. Critical points for the autonomous system.

Name	$x_{1c}$	$x_{2c}$	$x_{3c}$	$y_{1c}$	$y_{2c}$	$u_c$	$\varrho_c$
$a_R$	0	0	$x_{3c}$	0	0	0	$\sqrt{1-3x_{3c}^2}$
$b_R$	$\frac{2\sqrt{\frac{2}{3}}}{\lambda_1}$	0	$x_{3c}$	$\frac{2}{\sqrt{3}\lambda_1}$	0	0	$\frac{\sqrt{\lambda_1^2-3\lambda_1^2x_{3c}^2-4}}{\lambda_1}$
$c_M$	0	0	0	0	0	0	0
$d_M$	$\frac{\sqrt{\frac{3}{2}}}{\lambda_1}$	0	0	$\frac{\sqrt{\frac{3}{2}}}{\lambda_1}$	0	0	0
$e_{SM}$	1	0	0	0	0	0	0
$f$	0	0	0	$\frac{\sqrt{\sigma_1-3\sigma_1y_{3c}^2}}{\sqrt{\lambda_1+\sigma_1}}$	$y_{2c}$	$\frac{\lambda_1-3\lambda_1y_{2c}^2}{\lambda_1+\sigma_1}$	0
$g$	0	0	$x_{3c}$	$\frac{\sqrt{-3\lambda_2\sigma_1x_{3c}^2+\lambda_2\sigma_1-\sigma_1}}{\sqrt{\lambda_2\sigma_1+\lambda_1\lambda_2}}$	$\frac{1}{\sqrt{3}\sqrt{\lambda_2}}$	$\frac{-3\lambda_1\lambda_2x_{3c}^2-\lambda_1+\lambda_1\lambda_2}{\lambda_2(\lambda_1+\sigma_1)}$	0
$h$	0	0	0	$\frac{\sqrt{\sigma_1}}{\sqrt{\lambda_1+\sigma_1}}$	0	$\frac{\lambda_1}{\lambda_1+\sigma_1}$	0
$i$	$\frac{\lambda_1}{\sqrt{6}}$	0	0	$\frac{\sqrt{6-\lambda_1^2}}{\sqrt{6}}$	0	0	0
$j$	0	0	$\frac{\sqrt{\lambda_2-1}}{\sqrt{3}\sqrt{\lambda_2}}$	0	$\frac{1}{\sqrt{3}\sqrt{\lambda_2}}$	0	0

$p_{de}/\rho_{de}$  can be rewritten as

$$w_{de} = -(2\sqrt{6}\sigma_1ux_1 + u\varrho^2 - 36\lambda_2x_3^2y_2^2 + 3x_1^2 + 3x_2^2 + 3x_3^2 + 6x_2x_3 - 3y_1^2 - 9y_2^2)/(3(u-1)(u+x_1^2+3x_2^2+3x_3^2+6x_2x_3+y_1^2+3y_2^2)), \quad (45)$$

whereas the total equation of state becomes

$$w_{tot} = \frac{1}{3-3u}(2\sqrt{6}\sigma_1ux_1 - 36\lambda_2x_3^2y_2^2 + 3x_1^2 + 3x_2^2 + 3x_3^2 + 6x_2x_3 - 3y_1^2 - 9y_2^2 + \varrho^2). \quad (46)$$

To obtain an autonomous system from the dynamical system (41), we need to define the potentials of both the scalar and vector fields, as well as the non-minimal coupling function. From now we concentrate in the exponential potential  $V_1(\phi) \sim e^{-\kappa\lambda_1\phi}$  and  $V_2(A^2) \sim e^{-\kappa^2\lambda_2A^2}$ . This type of potential is known to allow scaling solutions [76]. Also, the most natural and simple choice for the nonminimal coupling function, which is compatible with the exponential scalar potential, is represented by the function  $F(\phi) \sim e^{-\kappa\sigma\phi}$  [78]. Below, we study the critical points and their stability properties.

### A. Critical points

We obtain the critical points from the conditions  $dx_1/dN = dx_2/dN = dx_3/dN = dy_1/dN = dy_2/dN = du/dN = d\varrho/dN = 0$ . Also, the definitions in Eq. (39) imply that the values of the critical points are real, with  $y_1 > 0$ ,  $y_2 > 0$ , and  $\varrho > 0$ . The critical points for system (41) are shown in Table I, and their values of cosmological parameters in Table II.

The critical point  $a_R$  represents a scaling radiation era with  $\Omega_{de}^{(r)} = 3x_{3c}^2$ . For  $x_{3c} = 0$  we recover the radiation-dominated solution with  $\Omega_r = 1$  and  $\omega_{de} = \omega_{tot} = 1/3$ .

Otherwise, to be consistent with the earliest constraint coming from the physics of big bang nucleosynthesis (BBN),  $\Omega_{de}^{(r)} < 0.045$  [79, 80], we require  $x_{3c} < 0.122$ . Point  $b_R$  also corresponds to a scaling radiation with  $\Omega_{de}^{(r)} = 3x_{3c}^2 + 4/\lambda_1^2$ . In this case, the radiation-dominated era can only be possible in the limit  $x_{3c} \rightarrow 0$  and  $\lambda_1 \rightarrow \pm\infty$ . On the other hand, the critical point  $c_M$  is a matter-dominated era with  $\Omega_m = 1$  and  $\omega_{de} = \omega_{tot} = 0$ . Critical point  $d_M$  describes a scaling matter era with  $\Omega_{de}^{(r)} = 3/\lambda_1^2$  and then the matter-dominated era is recovered for  $\lambda_1 \rightarrow \pm\infty$ .

Critical point  $e_{SM}$  is a dark energy-dominated solution with  $\Omega_{de} = 1$ . However, this solution cannot explain the current accelerated expansion because its equation of state is of the stiff matter type with  $\omega_{de} = \omega_{tot} = 1$ . Critical points  $f$ ,  $g$ ,  $h$  and  $j$  are also dark energy-dominated solutions with a de Sitter equation of state  $\omega_{de} = \omega_{tot} = -1$ . Therefore, these solutions provide accelerated expansion for all the values of parameters. Interestingly enough, points  $f$  and  $g$  have contributions from both the scalar and vector fields, while the points  $h$  and  $j$  only receive contribution from the scalar and vector fields, respectively. Finally, point  $i$  is a dark energy-dominated solution with an equation of state of the quintessence type with accelerated expansion for  $\lambda_1 < \sqrt{2}$ . This point corresponds to the standard accelerated solution for quintessence models [76].

### B. Stability of critical points

In this section we study the stability of the critical points. For this we assume time-dependent linear perturbations around each critical point, and from the autonomous system (41) the corresponding linear perturbation matrix  $\mathcal{M}$  is obtained [76]. The eigenvalues of  $\mathcal{M}$

evaluated at each fixed point give the stability conditions that we are looking for. Thus, we follow the standard classification of the stability properties: (i) Stable node: all the eigenvalues are negative; (ii) Unstable node: all the eigenvalues are positive; (iii) Saddle point: at least one is positive and the others are negative; (iv) Stable spiral: the determinant of  $\mathcal{M}$  is negative, and the real part of all the eigenvalues are negative. Points which are stable node or stable spiral are called attractor points, and these fixed points are reached through the cosmological evolution of the Universe, independently of the initial conditions.

TABLE II. Cosmological parameters for the critical points in Table I.

Name	$\Omega_{de}$	$\Omega_m$	$\Omega_r$	$\omega_{de}$	$\omega_{tot}$
$a_R$	$3x_{3c}^2$	0	$1 - 3x_{3c}^2$	$\frac{1}{3}$	$\frac{1}{3}$
$b_R$	$3x_{3c}^2 + \frac{4}{\lambda_1^2}$	0	$-3x_{3c}^2 - \frac{4}{\lambda_1^2} + 1$	$\frac{1}{3}$	$\frac{1}{3}$
$c_M$	0	1	0	0	0
$d_M$	$\frac{3}{\lambda_1^2}$	$1 - \frac{3}{\lambda_1^2}$	0	0	0
$e_{SM}$	1	0	0	1	1
$f$	1	0	0	-1	-1
$g$	1	0	0	-1	-1
$h$	1	0	0	-1	-1
$i$	1	0	0	$\frac{1}{3}(\lambda_1^2 - 3)$	$\frac{1}{3}(\lambda_1^2 - 3)$
$j$	1	0	0	-1	-1

Now, we analyze the corresponding eigenvalues for each critical point and their stability conditions.

- Point  $a_R$  has the eigenvalues

$$\begin{aligned} \mu_1 = 2, \quad \mu_2 = 2, \quad \mu_3 = -1, \quad \mu_4 = -1, \\ \mu_5 = 1, \quad \mu_6 = 0, \quad \mu_7 = 0. \end{aligned} \quad (47)$$

Since this critical point have positive and negative eigenvalues we can conclude that it is always unstable.

- Point  $b_R$  has the eigenvalues

$$\begin{aligned} \mu_1 = 0, \quad \mu_2 = -1, \quad \mu_3 = 1, \quad \mu_4 = 2, \\ \mu_5 = -\frac{\sqrt{64-15\lambda_1^2+\lambda_1}}{2\lambda_1}, \quad \mu_6 = \frac{\sqrt{64-15\lambda_1^2-\lambda_1}}{2\lambda_1}, \\ \mu_7 = -\frac{4\sigma_1}{\lambda_1}. \end{aligned} \quad (48)$$

For the same reason as for the point  $a_R$ , the point  $b_R$  is also always unstable.

- Point  $c_M$  has the eigenvalues

$$\begin{aligned} \mu_1 = -\frac{3}{2}, \quad \mu_2 = \frac{3}{2}, \quad \mu_3 = \frac{3}{2}, \quad \mu_4 = -1, \\ \mu_5 = -\frac{1}{2}, \quad \mu_6 = -\frac{1}{2}, \quad \mu_7 = 0. \end{aligned} \quad (49)$$

Similarly, this point is always unstable.

- Point  $d_M$  has the eigenvalues

$$\begin{aligned} \mu_1 = -1, \quad \mu_2 = -\frac{1}{2}, \quad \mu_3 = -\frac{1}{2}, \quad \mu_4 = \frac{3}{2}, \\ \mu_5 = -\frac{3(\sqrt{24-7\lambda_1^2+\lambda_1})}{4\lambda_1}, \quad \mu_6 = \frac{3(\sqrt{24-7\lambda_1^2-\lambda_1})}{4\lambda_1}, \\ \mu_7 = -\frac{3\sigma_1}{\lambda_1}. \end{aligned} \quad (50)$$

This point is always a saddle point for  $-2\sqrt{\frac{6}{7}} < \lambda_1 < 2\sqrt{\frac{6}{7}}$ .

- Point  $e_{SM}$  has the eigenvalues

$$\begin{aligned} \mu_1 = 3, \quad \mu_2 = 3, \quad \mu_3 = -1, \quad \mu_4 = 1, \\ \mu_5 = 1, \quad \mu_6 = 3 - \sqrt{\frac{3}{2}}\lambda_1, \quad \mu_7 = -\sqrt{6}\sigma_1. \end{aligned} \quad (51)$$

This point is always a saddle point.

- Point  $h$  has the eigenvalues

$$\begin{aligned} \mu_1 = 0, \quad \mu_2 = -1, \quad \mu_3 = -2, \quad \mu_4 = -2, \\ \mu_5 = -3, \quad \mu_6 = \frac{1}{2}(-\sqrt{12\lambda_1\sigma_1+9}-3), \\ \mu_7 = \frac{1}{2}(\sqrt{12\lambda_1\sigma_1+9}-3), \end{aligned} \quad (52)$$

where,

$$\begin{aligned} \left( \sigma_1 < 0 \wedge 0 < \lambda_1 \leq -\frac{3}{4\sigma_1} \right) \vee \\ \left( \sigma_1 > 0 \wedge -\frac{3}{4\sigma_1} \leq \lambda_1 < 0 \right), \end{aligned} \quad (53)$$

to be marginally stable.

- Point  $i$  has the eigenvalues

$$\begin{aligned} \mu_1 = -1, \quad \mu_2 = \frac{\lambda_1^2}{2}, \quad \mu_3 = \frac{1}{2}(\lambda_1^2 - 6), \\ \mu_4 = \frac{1}{2}(\lambda_1^2 - 4), \quad \mu_5 = \frac{1}{2}(\lambda_1^2 - 4), \quad \mu_6 = \lambda_1^2 - 3, \\ \mu_7 = -\lambda_1\sigma_1. \end{aligned} \quad (54)$$

This point is always a saddle point.

- Point  $j$  has the eigenvalues

$$\begin{aligned} \mu_1 = 0, \quad \mu_2 = 0, \quad \mu_3 = -3, \quad \mu_4 = -3, \\ \mu_5 = -2, \quad \mu_6 = -\frac{\sqrt{-\lambda_2(7\lambda_2-16)+3\lambda_2}}{2\lambda_2}, \\ \mu_7 = \frac{\sqrt{-\lambda_2(7\lambda_2-16)-3\lambda_2}}{2\lambda_2}, \end{aligned} \quad (55)$$

where,

$$1 < \lambda_2 \leq \frac{16}{7}, \quad (56)$$

to be marginally stable.

The eigenvalues associated to critical points  $f$  and  $g$  are quite long, and we add them to appendix A. We found that at linear order, these critical points are also marginally stable. In Section VI we verify numerically that they are indeed stable fixed points.

Below we perform a numerical integration of the autonomous system to corroborate our analytical results.

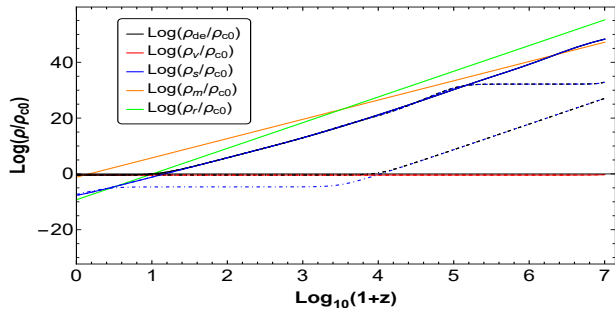


FIG. 1. We depict the evolution of the energy density of dark energy  $\rho_{de}$  (black), scalar field density  $\rho_s$  (blue), vector field density  $\rho_v$  (red), dark matter (including baryons)  $\rho_m$  (orange) and radiation  $\rho_r$  (green) as functions of the redshift  $z$ , for  $\lambda_1 = 5.5 \times 10^1$ ,  $\lambda_2 = 1$  and  $\sigma_1 = 10^{-1}$ . In particular, solid lines correspond to initial conditions  $x_{1i} = 0.0222681$ ,  $x_{2i} = 10^{-13}$ ,  $x_{3i} = 10^{-13}$ ,  $y_{1i} = 0.0222681$ ,  $y_{2i} = 0.485 \times 10^{-12}$ ,  $u_i = 6 \times 10^{-13}$  and  $\varrho_i = 0.999339$ . Dashed lines correspond to initial conditions  $x_{1i} = 10^{-5}$ ,  $x_{2i} = 10^{-13}$ ,  $x_{3i} = 10^{-13}$ ,  $y_{1i} = 10^{-5}$ ,  $y_{2i} = 0.485 \times 10^{-12}$ ,  $u_i = 6 \times 10^{-13}$  and  $\varrho_i = 0.99983$ . Dot-dashed lines correspond to initial conditions  $x_{1i} = 10^{-13}$ ,  $x_{2i} = 10^{-13}$ ,  $x_{3i} = 10^{-13}$ ,  $y_{1i} = 10^{-13}$ ,  $y_{2i} = 0.485 \times 10^{-12}$ ,  $u_i = 6 \times 10^{-13}$  and  $\varrho_i = 0.99983$ . During the scaling radiation era  $a_R$  we obtained  $\Omega_{de}^{(r)} \approx 9.91736 \times 10^{-4}$ , while in the case of  $b_R$  we found  $\Omega_{de}^{(r)} \approx 1.66852 \times 10^{-3}$ . Also, during the scaling matter era  $d_M$ , we got  $\Omega_{de}^{(m)} \approx 1.00912 \times 10^{-3}$  at redshift  $z = 50$ .

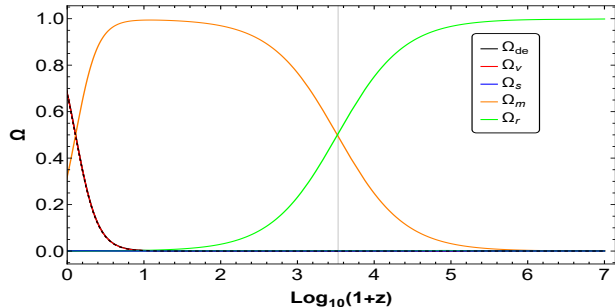


FIG. 2. The evolution of the fractional energy densities for the same initial conditions used in figure 1. Where we can observe that the fractional energy density of dark energy (black line) and the fractional energy density related to vector field (red line) are overlapping, and the fractional energy density related to scalar field is around  $10^{-4}$  (blue line). Also, the time of radiation-matter equality is around  $z \approx 3387$ . Finally, at future times,  $\Omega_v \approx 0.999946$  and  $\Omega_s \approx 5.37922 \times 10^{-5}$ .

## VI. NUMERICAL RESULTS

We found five critical points that allow an accelerated expansion,  $f, g, h, i$  and  $j$ . And we have verified numerically that the points  $f, g, h$ , and  $j$  are attractors. However, the critical point  $i$ , which is related to the ordinary exponential quintessence model [76, 77] is no longer a stable point, Eq. (54).

In FIG. 7, we show the evolution of the system in the phase space through the trajectories  $a_R \rightarrow c_M \rightarrow f$ ,  $a_R \rightarrow d_M \rightarrow f$  and  $b_R \rightarrow d_M \rightarrow f$ . In FIG. 1 it is

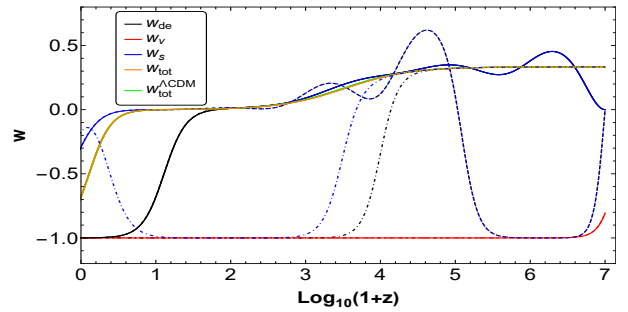


FIG. 3. We depict the equation of state  $w_{tot}$  (orange line), the EOS of dark energy  $w_{de}$  (black line), the EOS related to vector field  $w_v$  (red line), the EOS related to scalar field  $w_s$  (blue line), and the total EOS of  $\Lambda\text{CDM}$  model as redshift functions. Also, we used the same initial conditions of figure 1 to obtain the solid, dashed, and dot-dashed blue lines and red lines. Finally, we obtain the value  $w_{de} = -0.999516$  at  $z = 0$ , in accordance with  $w_{de}^{(0)} = -1.028 \pm 0.032$ , from Planck data [81].

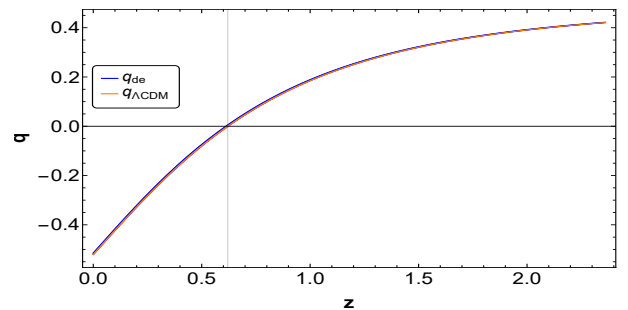


FIG. 4. We show the evolution of the deceleration parameter  $q(z)$ , for the same initial conditions used in figure 1. The transition to dark energy dominance is around  $z \approx 0.62$ , consistent with current observational data.

depicted the evolution of the energy densities of dark energy, dark matter and radiation, along with the vector and the scalar components of dark energy. Thus, one can verify that there exists for these trajectories a scaling regime of the fields during the radiation and matter eras. Furthermore, in FIG. 2 we plot the behavior of the corresponding fractional energy densities for the same initial conditions that in FIG 1, showing that the nature of the final attractor is purely vectorial. At the present time, redshift  $z = 0$ , we found  $\Omega_{de}^{(0)} \approx 0.68$  and dark matter  $\Omega_m^{(0)} \approx 0.32$ , which is consistent with observations.

In FIG. 3 we show the cosmic evolution of the total EOS, the EOS of dark energy, and the EOS parameter of the vectorial and scalar components of dark energy. To compare with the current concordance model, we also added the evolution curve of the EOS of the  $\Lambda\text{CDM}$  model. For the EOS parameter of dark energy at  $z = 0$  we obtained  $w_{de}(z = 0) \approx -0.999516$ , which is in agreement with the observational constraint  $w_{de}^{(0)} = -1.028 \pm 0.032$  [82]. From FIG. 2 one can check that the time of radiation-matter equality is around

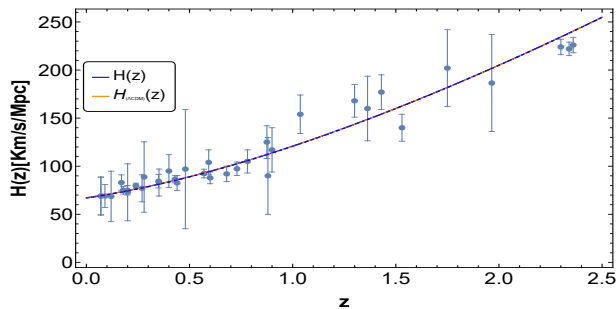


FIG. 5. We present the variation of the Hubble rate, denoted as  $H(z)$ , in relation to the redshift  $z$ . The observed data points for the Hubble rate are depicted as blue points, accompanied by their corresponding  $1\sigma$  confidence intervals, as detailed in Table III. We utilize identical initial conditions as displayed in FIG 1 to generate the solid, dashed, and dot-dashed blue lines. By comparing the theoretical model predictions represented by these lines with the observed data, we can assess the level of agreement between the empirical measurements of the Hubble rate at different redshifts and the theoretical model.

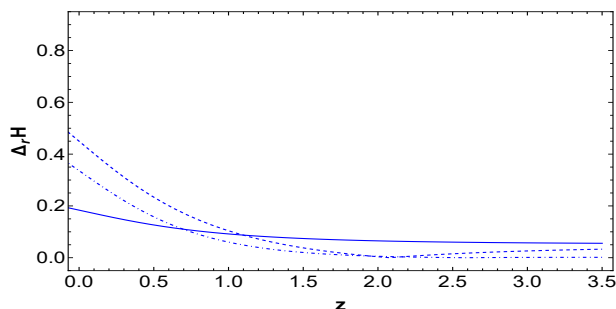


FIG. 6. The figure illustrates the relative difference (expressed as a percentage), denoted as  $\Delta_r H(z) = 100 \times |H - H_{\Lambda CDM}| / H_{\Lambda CDM}$ , in comparison to the  $\Lambda$ CDM model. The solid, dashed, and dot-dashed blue lines are derived from the identical initial conditions presented in FIG. 1, are utilized in this analysis. By evaluating the relative difference between the Hubble rate  $H$  and the Hubble rate of the  $\Lambda$ CDM model  $H_{\Lambda CDM}$ , we can examine the deviations from the  $\Lambda$ CDM model and the associated significance at different redshifts.

$z \approx 3387$ . Moreover, in FIG. 4 we depict the deceleration parameter for the same initial conditions. This plot shows that the transition to the accelerated phase occurs at  $z \approx 0.62$ , which is very close to the  $\Lambda$ CDM value.

It is important to mention that for the scaling radiation/matter regimes, we have respected the constraints coming from both the Physics of Big Bang Nucleosynthesis (BBN),  $\Omega_{de}^{(r)} < 0.045$ , [80], and CMB measurements from Planck,  $\Omega_{de}^{(m)} < 0.02$  (95% CL) at redshift  $z = 50$  [83]. For instance, in FIG 1, during the scaling radiation era  $a_R$  we obtained  $\Omega_{de}^{(r)} \approx 9.91736 \times 10^{-4}$ , while in the case of  $b_R$  we found  $\Omega_{de}^{(r)} \approx 1.66852 \times 10^{-3}$ . Also, during the scaling matter era  $d_M$ , we got  $\Omega_{de}^{(m)} \approx 1.00912 \times 10^{-3}$  at redshift  $z = 50$ .

In FIGS. 14 and 21 we depict the evolution curves in the phase space for the transitions  $a_R \rightarrow c_M \rightarrow f$ ,  $a_R \rightarrow c_M \rightarrow g$ ,  $a_R \rightarrow c_M \rightarrow d_M \rightarrow f$ , and  $a_R \rightarrow b_R \rightarrow d_R \rightarrow f$ , for another set of parameter values and initial conditions. The corresponding behavior of the energy

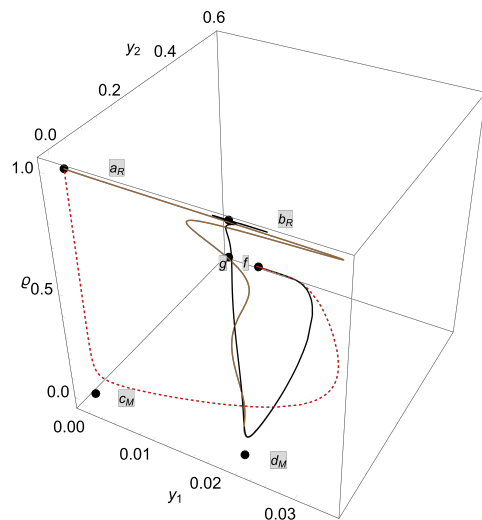


FIG. 7. Evolution curves in the phase space for  $\lambda_1 = 5.5 \times 10^1$ ,  $\lambda_2 = 1$  and  $\sigma_1 = 10^{-1}$ . Black solid line correspond to initial conditions  $x_{1i} = 0.0222681$ ,  $x_{2i} = 10^{-13}$ ,  $x_{3i} = 10^{-13}$ ,  $y_{1i} = 0.0222681$ ,  $y_{2i} = 0.485 \times 10^{-12}$ ,  $u_i = 6 \times 10^{-13}$  and  $\varrho_i = 0.999339$ . Brown solid line correspond to initial conditions  $x_{1i} = 10^{-5}$ ,  $x_{2i} = 10^{-13}$ ,  $x_{3i} = 10^{-13}$ ,  $y_{1i} = 10^{-5}$ ,  $y_{2i} = 0.485 \times 10^{-12}$ ,  $u_i = 6 \times 10^{-13}$  and  $\varrho_i = 0.99983$ . Red dashed line correspond to initial conditions  $x_{1i} = 10^{-13}$ ,  $x_{2i} = 10^{-13}$ ,  $x_{3i} = 10^{-13}$ ,  $y_{1i} = 10^{-13}$ ,  $y_{2i} = 0.485 \times 10^{-12}$ ,  $u_i = 6 \times 10^{-13}$  and  $\varrho_i = 0.99983$ .

densities of dark energy, dark matter and radiation are shown in FIGS. 8, 9, 15 and 16. Moreover, the cosmic evolution of the EOS parameter of dark energy and the total EOS are shown in FIGS 10 and 17. In these figures, we also depicted the behavior of the vector and scalar fields. Finally, the evolution of the deceleration parameter is presented in FIGS. 11 and 18.

We choose parameters  $\lambda_1$ ,  $\lambda_2$ , and  $\sigma$  based on the stability conditions of critical points and observational constraints. Specifically, we numerically solve the dynamical system (41) using three sets of values for the parameters  $\lambda_1$ ,  $\lambda_2$ , and  $\sigma$ , as well as initial conditions (values given in Fig. 1, Fig. 8, and Fig. 15). These values are selected to ensure the stability of points  $f$  and  $g$  (Fig. 7, Fig. 14, and Fig. 21) and to be consistent with the observational values:  $\Omega_{DE} \approx 0.68$  (Fig. 2, Fig. 9, and Fig. 16),  $w_{de}^{(0)} = -1.028 \pm 0.032$  (Fig. 3, Fig. 10, and Fig. 17), radiation-matter equality around  $z \approx 3387$  (Fig. 2, Fig. 9, and Fig. 16), and transition to dark energy dominance around  $z \approx 0.62$  (Fig. 4, Fig. 11, and Fig. 18). Even more, our numerical solutions (Fig. 2, Fig. 9, and Fig. 16) are consistent with constraints arising from Big Bang Nucleosynthesis (BBN) and measurements obtained from the Cosmic Microwave Background (CMB) by the Planck satellite. That is to say, according to BBN,  $\Omega_{de}^{(r)}$  is limited to  $\Omega_{de}^{(r)} < 0.045$  ( $2\sigma$  C.L.) [80], while CMB measurements at a redshift of approximately  $z \approx 50$  from Planck indicate  $\Omega_{de}^{(m)} < 0.02$  ( $2\sigma$  C.L.) [83]. Finally, it is important to note that the next step involves identifying the best-fit parameters of  $\lambda_1$ ,  $\lambda_2$ , and  $\sigma$  and determining

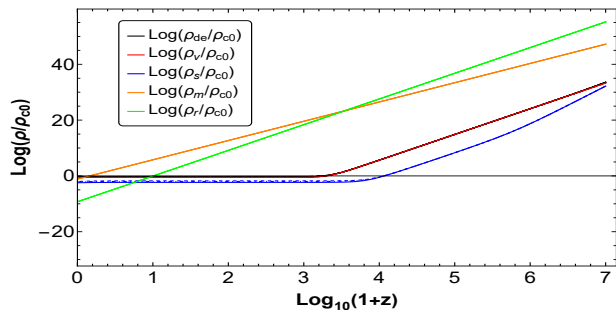


FIG. 8. We depict the evolution of the energy density of dark energy  $\rho_{\text{de}}$  (black), scalar field density  $\rho_s$  (blue), vector field density  $\rho_v$  (red), dark matter (including baryons)  $\rho_m$  (orange) and radiation  $\rho_r$  (green) as functions of the redshift  $z$ , for  $\lambda_1 = 2.2$ ,  $\lambda_2 = 1$  and  $\sigma_1 = 1$ . In particular, solid lines correspond to initial conditions  $x_{1i} = 10^{-5}$ ,  $x_{2i} = 10^{-13}$ ,  $x_{3i} = 10^{-13}$ ,  $y_{1i} = 3.2 \times 10^{-13}$ ,  $y_{2i} = 4.5 \times 10^{-13}$ ,  $u_i = 4 \times 10^{-13}$  and  $\varrho_i = 0.99983$ . Dashed lines correspond to initial conditions  $x_{1i} = 10^{-5}$ ,  $x_{2i} = 10^{-5}$ ,  $x_{3i} = 10^{-13}$ ,  $y_{1i} = 4.2 \times 10^{-13}$ ,  $y_{2i} = 4.5 \times 10^{-13}$ ,  $u_i = 4 \times 10^{-13}$  and  $\varrho_i = 0.99983$ . Dot-dashed lines correspond to initial conditions  $x_{1i} = 10^{-5}$ ,  $x_{2i} = 10^{-13}$ ,  $x_{3i} = 10^{-13}$ ,  $y_{1i} = 3.8 \times 10^{-13}$ ,  $y_{2i} = 4.5 \times 10^{-13}$ ,  $u_i = 4.0 \times 10^{-13}$  and  $\varrho_i = 0.99983$ . During the scaling radiation era  $a_R$  we obtained  $\Omega_{\text{de}}^{(r)} \approx 4.004 \times 10^{-10}$ .

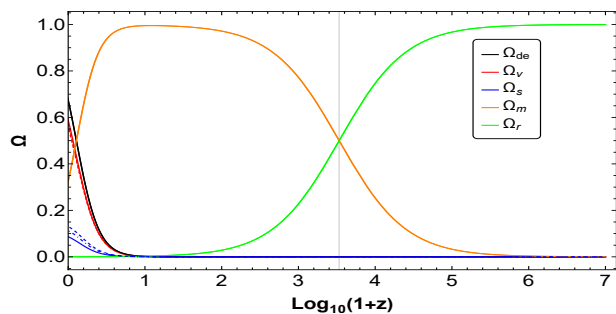


FIG. 9. The evolution of the fractional energy densities of dark energy (black line), vector field (red line) and scalar field (blue line), for the same initial conditions used in figure 8. Also, the time of radiation-matter equality is around  $z \approx 3387$ . Finally, at future times,  $\Omega_v \approx 0.96571$  and  $\Omega_s \approx 3.42898 \times 10^{-2}$ .

their corresponding confidence intervals through statistical analysis. However, conducting this analysis exceeds the scope of this paper. But, with these previous results, we have proved that the model satisfies the preliminary requirements to be considered viable [82].

## VII. HUBBLE PARAMETER $H(z)$

To analyze the behavior of the Hubble rate and its confidence interval, we will utilize a set of 39 data points obtained from previous studies [84, 85]. These data points, expressed in terms of redshift  $z$ , are presented in Table III. Moreover, to facilitate further comparisons, we employ the  $\Lambda$ CDM model, which provides a Hubble rate varying with redshift according to the following expres-

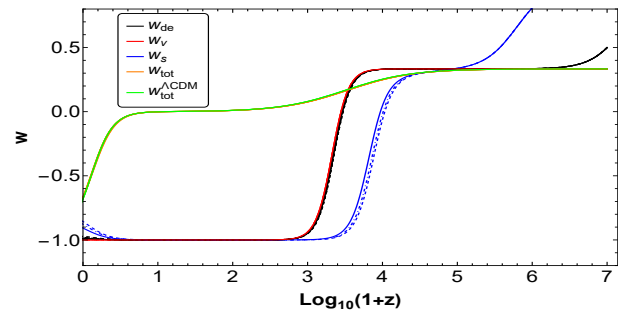


FIG. 10. We depict the equation of state  $w_{\text{tot}}$  (orange line), the EOS of dark energy  $w_{\text{de}}$  (black line), the EOS related to vector field  $w_v$  (red line), the EOS related to scalar field  $w_s$  (blue line), and the total EOS of  $\Lambda$ CDM model (green line) as redshift functions. Also, we used the same initial conditions of figure 9 to obtain the solid, dashed, and dot-dashed blue lines and red lines. Finally, we obtain the value  $w_{\text{de}} = -0.996$  at  $z = 0$ , in accordance with  $w_{\text{de}}^{(0)} = -1.028 \pm 0.032$ , from Planck data [81].

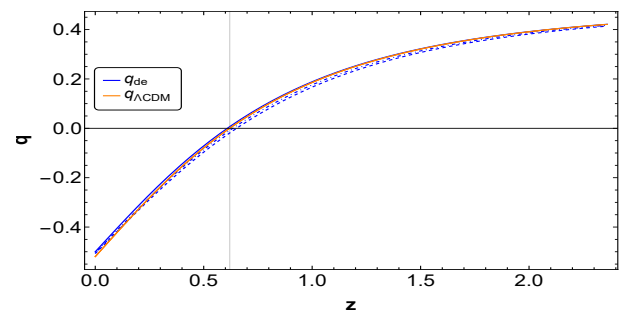


FIG. 11. We show the evolution of the deceleration parameter  $q(z)$ , for the same initial conditions used in figure 1. Where, the transition to dark energy dominance is around  $z \approx 0.62$ , which is consistent with current observational data.

sion:

$$H_{\Lambda\text{CDM}}(z) = H_0 \sqrt{\Omega_{\text{de}}^{(0)} + \Omega_m^{(0)}(1+z)^3 + \Omega_r^{(0)}(1+z)^4}. \quad (57)$$

Figures 5, 12 and 19 illustrate the evolution of the Hubble rate as a function of redshift for our model. The parameter values and initial conditions utilized for Figures 1, 8 and 15 are consistent with those employed for the aforementioned plots. We compare these results with the standard outcomes obtained from the  $\Lambda$ CDM model and the current observational data on the Hubble rate  $H(z)$ . Consequently, we conclude that our findings align with observational  $H(z)$  data. To further evaluate the consistency between our model and  $\Lambda$ CDM, we examine the relative difference, denoted as  $\Delta_r H(z)$ , between the results obtained from our model and  $\Lambda$ CDM. Figures 6, 13 and 20 provide a visualization of this comparison, indicating that our results closely resemble those of  $\Lambda$ CDM.

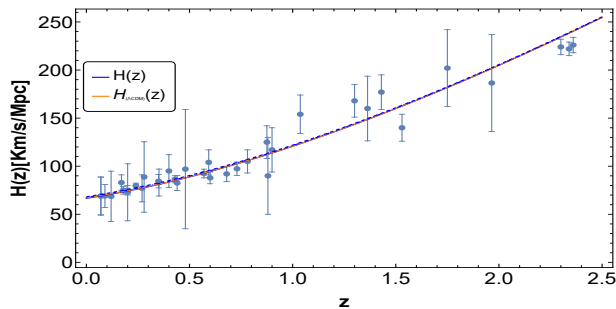


FIG. 12. We present the variation of the Hubble rate, denoted as  $H(z)$ , in relation to the redshift  $z$ . The observed data points for the Hubble rate are depicted as blue points, accompanied by their corresponding  $1\sigma$  confidence intervals, as detailed in Table III. We utilize identical initial conditions as displayed in FIG 8 to generate the solid, dashed, and dot-dashed blue lines. By comparing the theoretical model predictions represented by these lines with the observed data, we can assess the level of agreement between the empirical measurements of the Hubble rate at different redshifts and the theoretical model.

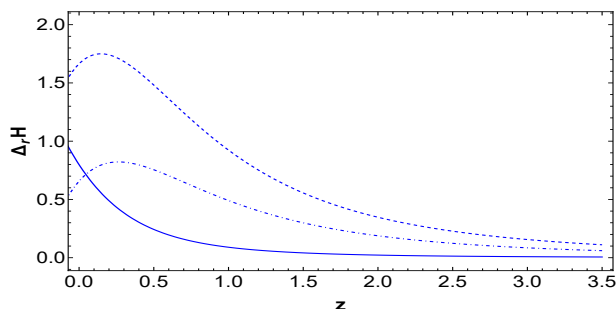


FIG. 13. The figure illustrates the relative difference (expressed as a percentage), denoted as  $\Delta_r H(z) = 100 \times |H - H_{\Lambda\text{CDM}}|/H_{\Lambda\text{CDM}}$ , in comparison to the  $\Lambda\text{CDM}$  model. The solid, dashed, and dot-dashed blue lines are derived from the identical initial conditions presented in FIG. 8, are utilized in this analysis. By evaluating the relative difference between the Hubble rate  $H$  and the Hubble rate of the  $\Lambda\text{CDM}$  model  $H_{\Lambda\text{CDM}}$ , we can examine the deviations from the  $\Lambda\text{CDM}$  model and the associated significance at different redshifts.

### VIII. DISCUSSIONS AND FINAL REMARKS

We investigated the cosmological dynamics of dark energy in a scalar-vector-torsion model [72], where the vector part is described by the cosmic triad, the scalar field is of quintessence type, and the torsion is associated to the Weitzenböck connection of teleparallel gravity [18–25]. We performed an exhaustive phase analysis looking for the critical points of the autonomous system and their stability properties [76].

In order to find the set of cosmological equations that govern the dynamics of the fields, we have assumed the FLRW background in the presence of radiation and cold dark matter fluids. We obtained the effective energy and pressure densities of dark energy and identified contributions from both the vector and scalar fields. In this way, we derived the autonomous system from this set of cosmological equations, and the corresponding critical points are shown in Table I. Furthermore, in Table II, we presented for each fixed point the results obtained for the

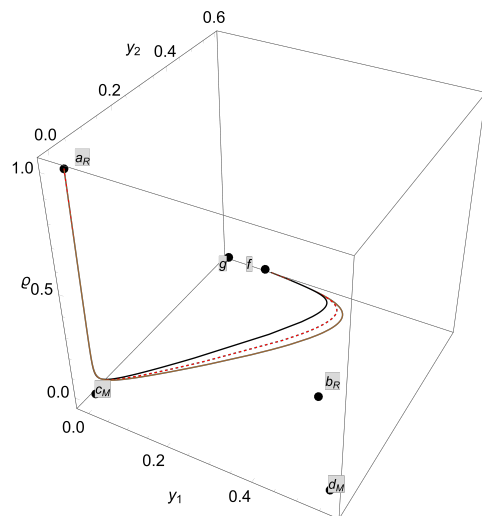


FIG. 14. Evolution curves in the phase space for  $\lambda_1 = 2.2$ ,  $\lambda_2 = 1$  and  $\sigma_1 = 1$ . Black solid line correspond to initial conditions  $x_{1i} = 10^{-5}$ ,  $x_{2i} = 10^{-5}$ ,  $x_{3i} = 10^{-13}$ ,  $y_{1i} = 3.2 \times 10^{-13}$ ,  $y_{2i} = 4.5 \times 10^{-13}$ ,  $u_i = 4 \times 10^{-13}$  and  $\varrho_i = 0.99983$ . Brown solid line correspond to initial conditions  $x_{1i} = 10^{-5}$ ,  $x_{2i} = 10^{-5}$ ,  $x_{3i} = 10^{-13}$ ,  $y_{1i} = 4.2 \times 10^{-13}$ ,  $y_{2i} = 4.5 \times 10^{-13}$ ,  $u_i = 4 \times 10^{-13}$  and  $\varrho_i = 0.99983$ . Red dot-dashed line correspond to initial conditions  $x_{1i} = 10^{-5}$ ,  $x_{2i} = 10^{-5}$ ,  $x_{3i} = 10^{-13}$ ,  $y_{1i} = 3.8 \times 10^{-13}$ ,  $y_{2i} = 4.5 \times 10^{-13}$ ,  $u_i = 4.0 \times 10^{-13}$  and  $\varrho_i = 0.99983$ .

relevant cosmological parameters. So, by numerically integrating the autonomous system we have corroborated all our analytical results. Particularly, we have shown that the dark energy model studied here, which is based on a scalar-vector-torsion gravity theory, is cosmologically viable and capable of successfully reproducing the thermal history of the universe. We found new attractor points, which are dark energy-dominated solutions with accelerated expansion. For these critical points, the fractional energy density of dark energy is composed of contributions coming from both the scalar and vector field densities. Thus, the dynamics of dark energy is driven by the two fields. The vector field behaves close to the cosmological constant, while the scalar field remains in the quintessence regime. Nevertheless, at late times we found that the energy density of the scalar field is always subdominant, and therefore the nature of dark energy could be mainly vectorial.

We also obtained new scaling solutions in which the scalar and vector field densities scale in the same way as the radiation and matter background fluids. After performing the stability analysis, we found that they are unstable fixed points without accelerated expansion. Although the vector field density only can scale as radiation and not matter, the scalar field can mimic both [77]. Also, it is important to note that scaling solutions are attractive once they can naturally incorporate early dark energy. They provide us with a mechanism to alleviate the energy scale problem of the  $\Lambda\text{CDM}$  model, which is related to the large energy gap that exists between the current critical energy density and the typical

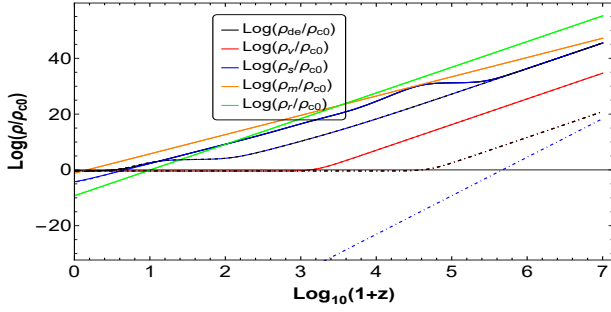


FIG. 15. We depict the evolution of the energy density of dark energy  $\rho_{de}$  (black), scalar field density  $\rho_s$  (blue), vector field density  $\rho_v$  (red), dark matter (including baryons)  $\rho_m$  (orange) and radiation  $\rho_r$  (green) as functions of the redshift  $z$ , for  $\lambda_1 = 10$ ,  $\lambda_2 = 1$  and  $\sigma_1 = 10$ . In particular, solid lines correspond to initial conditions  $x_{1i} = 10^{-5}$ ,  $x_{2i} = 10^{-5}$ ,  $x_{3i} = 10^{-5}$ ,  $y_{1i} = 6 \times 10^{-6}$ ,  $y_{2i} = 4.8 \times 10^{-13}$ ,  $u_i = 6 \times 10^{-5}$  and  $\rho_i = 0.99983$ . Dashed lines correspond to initial conditions  $x_{1i} = 10^{-5}$ ,  $x_{2i} = 10^{-5}$ ,  $x_{3i} = 10^{-5}$ ,  $y_{1i} = 6 \times 10^{-12}$ ,  $y_{2i} = 4.8 \times 10^{-13}$ ,  $u_i = 6 \times 10^{-5}$  and  $\rho_i = 0.99983$ . Dot-dashed lines correspond to initial conditions  $x_{1i} = 10^{-8}$ ,  $x_{2i} = 10^{-8}$ ,  $x_{3i} = 10^{-8}$ ,  $y_{1i} = 0$ ,  $y_{2i} = 4.9 \times 10^{-13}$ ,  $u_i = 0$  and  $\rho_i = 0.99983$ . During the scaling radiation era  $a_R$  we obtained  $\Omega_{de}^{(r)} \approx 6.00013 \times 10^{-5}$ , while in the case of  $b_R$  we found  $\Omega_{de}^{(r)} \approx 6.07537 \times 10^{-5}$ . Also, during the scaling matter era  $d_M$ , we got  $\Omega_{de}^{(m)} \approx 1.93572 \times 10^{-2}$  at redshift  $z = 50$ .

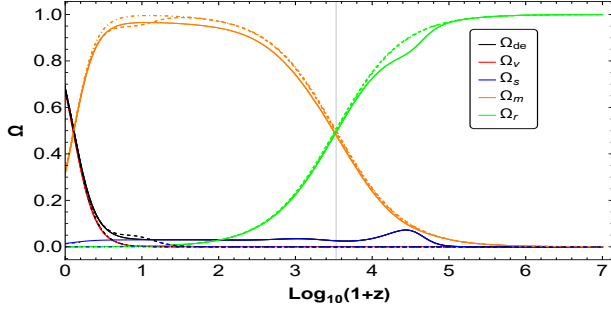


FIG. 16. The evolution of the fractional energy densities of dark energy (black line), vector field (red line) and scalar field (blue line), for the same initial conditions used in figure 9. Also, the time of radiation-matter equality is around  $z \approx 3387$ . Finally, at future times,  $\Omega_v \approx 0.998365$  and  $\Omega_s \approx 1.63459 \times 10^{-3}$ .

energy scales of particle physics [86, 87].

We found that the effective dark energy, comprising the energy densities of the scalar and vector fields, can exhibit scaling behavior in the early universe. This implies the existence of a small portion of dark energy contributing to the dynamics of the universe during the radiation and matter eras. It is important to note that both the vector and the scalar can drive this scaling behavior during the radiation era, while in the matter era, only the scalar field can provide this effect. This is a natural outcome, as an oscillating field can indeed act like an effective fluid with a constant equation of state, which has radiation-like or matter-like behavior depending on the potential [88]. Moreover, the dynamics of the vector field

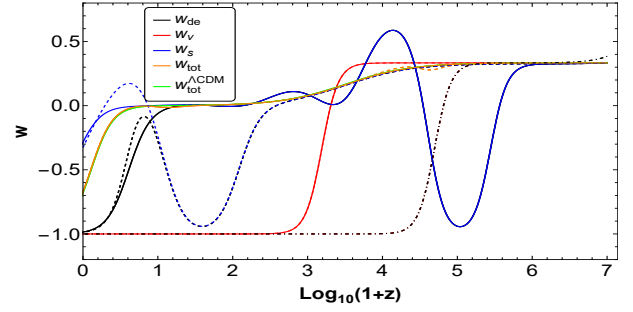


FIG. 17. We depict the equation of state  $w_{tot}$  (orange line), the EOS of dark energy  $w_{de}$  (black line), the EOS related to vector field  $w_v$  (red line), the EOS related to scalar field  $w_s$  (blue line), and the total EOS of  $\Lambda$ CDM model (green line) as redshift functions. Also, we used the same initial conditions of figure 9 to obtain the solid, dashed, and dot-dashed blue lines and red lines. Finally, we obtain the value  $w_{de} = -0.997323$  at  $z = 0$ .

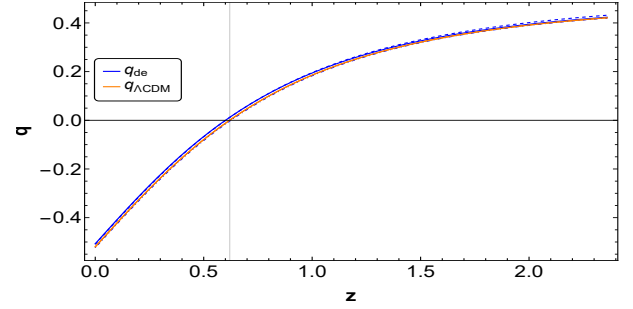


FIG. 18. We show the evolution of the deceleration parameter  $q(z)$ , for the same initial conditions used in figure 1. Where, the transition to dark energy dominance is around  $z \approx 0.62$ , which is consistent with current observational data.

resemble that of a Maxwell-type field [69].

Since the scaling solutions lead to the presence of small amounts of dark energy during the radiation and matter era, significant physical consequences can emerge [86, 87]. Specifically, it alters the Hubble rate during this period, thereby affecting the theoretical predictions for the abundances of primordial light elements [79, 80]. Moreover, a scaling field significantly impacts the shape of the spectrum of Cosmic Microwave Background (CMB) anisotropies [80]. This scaling field also influences the formation of large-scale structures in the universe, impacting the growth of cosmic structures such as galaxies and clusters of galaxies [89]. In this latter case, the effects on the matter power spectrum arise from the reduction of the matter fluctuation variance  $\sigma_8$ , due to the suppressed growth rate of matter perturbations [89–91]. Utilizing the latest observational data from Big Bang Nucleosynthesis and observed abundances of primordial nuclides, the authors in Ref. [80] established a strong constraint  $\Omega_{de} < 0.045$  at  $2\sigma$  C.L. for the permissible amount of dark energy during the radiation era. Additionally, based on CMB measurements [83], the constraint for the field energy density during the matter scaling epoch is

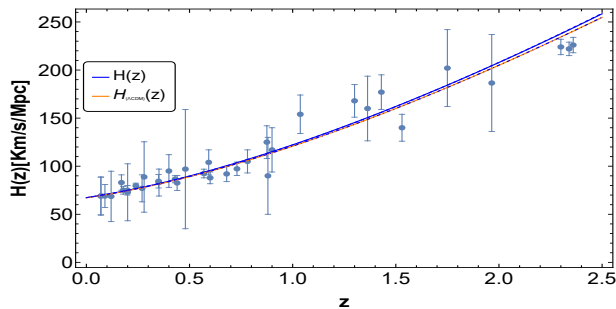


FIG. 19. We present the variation of the Hubble rate, denoted as  $H(z)$ , in relation to the redshift  $z$ . The observed data points for the Hubble rate are depicted as blue points, accompanied by their corresponding  $1\sigma$  confidence intervals, as detailed in Table III. We utilize identical initial conditions as displayed in FIG 15 to generate the solid, dashed, and dot-dashed blue lines. By comparing the theoretical model predictions represented by these lines with the observed data, we can assess the level of agreement between the empirical measurements of the Hubble rate at different redshifts and the theoretical model.

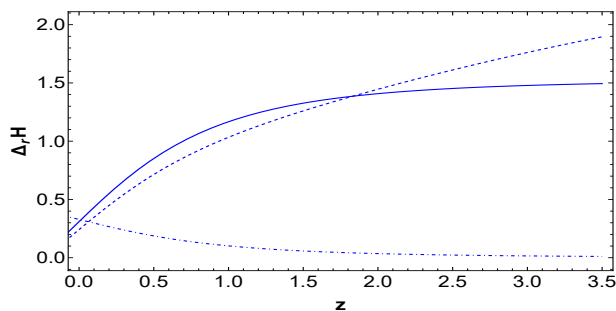


FIG. 20. The figure illustrates the relative difference (expressed as a percentage), denoted as  $\Delta_r H(z) = 100 \times |H - H_{\Lambda CDM}| / H_{\Lambda CDM}$ , in comparison to the  $\Lambda$ CDM model. The solid, dashed, and dot-dashed blue lines are derived from the identical initial conditions presented in FIG. 15, are utilized in this analysis. By evaluating the relative difference between the Hubble rate  $H$  and the Hubble rate of the  $\Lambda$ CDM model  $H_{\Lambda CDM}$ , we can examine the deviations from the  $\Lambda$ CDM model and the associated significance at different redshifts.

$\Omega_{de} < 0.02$  ( $2\sigma$  C.L.) at redshift  $z \approx 50$ . In our study, we used these values to constrain the model parameters when numerically solving our cosmological equations. Although this approach is valid and sufficient from a practical standpoint, for greater precision, we could further investigate the dynamics of the field density during early times to better predict the primordial abundances and the evolution of the cosmological perturbations. However, these additional studies are beyond the scope of the current work and will be the focus of future projects.

Finally, in order to decide whether or not the present model is a good candidate to describe nature, more studies are required. Particularly, these studies should

include a detailed observational confrontation, using data from Type Ia Supernovae (SNIa), Baryon Acoustic Oscillations (BAO) and Cosmic Microwave Background (CMB) observations. Also, a detailed perturbation analysis to investigate the matter clustering behavior, and the  $\sigma_8$  tension, would be essential [7–10]. These interesting and necessary studies lie beyond the scope of

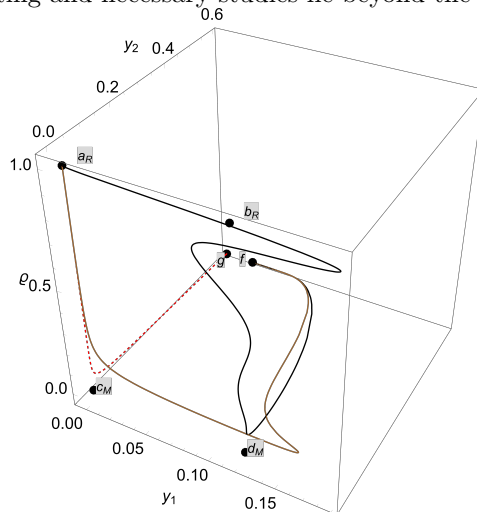


FIG. 21. Evolution curves in the phase space for  $\lambda_1 = 10$ ,  $\lambda_2 = 1$  and  $\sigma_1 = 10$ . Black solid line correspond to initial conditions  $x_{1i} = 10^{-5}$ ,  $x_{2i} = 10^{-5}$ ,  $x_{3i} = 10^{-5}$ ,  $y_{1i} = 6 \times 10^{-6}$ ,  $y_{2i} = 4.8 \times 10^{-13}$ ,  $u_i = 6 \times 10^{-5}$  and  $\varrho_i = 0.99983$ . Brown solid line correspond to initial conditions  $x_{1i} = 10^{-5}$ ,  $x_{2i} = 10^{-5}$ ,  $x_{3i} = 10^{-5}$ ,  $y_{1i} = 6 \times 10^{-12}$ ,  $y_{2i} = 4.8 \times 10^{-13}$ ,  $u_i = 6 \times 10^{-5}$  and  $\varrho_i = 0.99983$ . Red dot-dashed line correspond to initial conditions  $x_{1i} = 10^{-8}$ ,  $x_{2i} = 10^{-8}$ ,  $x_{3i} = 10^{-8}$ ,  $y_{1i} = 0$ ,  $y_{2i} = 4.9 \times 10^{-13}$ ,  $u_i = 0$  and  $\varrho_i = 0.99983$ .

the present work and are left for future projects.

**Data availability:** There are no new data associated with this article.

## ACKNOWLEDGMENTS

M. Gonzalez-Espinoza acknowledges the financial support of FONDECYT de Postdoctorado, N° 3230801. Y. Leyva acknowledges Dirección de Investigación, Postgrado y Transferencia Tecnológica de la Universidad de Tarapacá for financial support through Proyecto “Fortalecimiento Grupos de Investigación UTA Código N° 4732-23”. G. Otorola and J. Saavedra acknowledge the financial support of Fondecyt Grant 1220065.

[1] A. G. Riess *et al.* (Supernova Search Team), Observational evidence from supernovae for an accelerating uni-

verse and a cosmological constant, *Astron. J.* **116**, 1009 (1998), arXiv:astro-ph/9805201 [astro-ph].

- [2] S. Perlmutter *et al.* (Supernova Cosmology Project), Measurements of Omega and Lambda from 42 high redshift supernovae, *Astrophys. J.* **517**, 565 (1999), arXiv:astro-ph/9812133 [astro-ph].
- [3] F. Zwicky, Die Rotverschiebung von extragalaktischen Nebeln, *Helv. Phys. Acta* **6**, 110 (1933).
- [4] S. Weinberg, The Cosmological Constant Problem, *Rev. Mod. Phys.* **61**, 1 (1989).
- [5] S. M. Carroll, The Cosmological constant, *Living Rev. Rel.* **4**, 1 (2001), arXiv:astro-ph/0004075.
- [6] A. Padilla, Lectures on the Cosmological Constant Problem, arXiv:1502.05296 (2015), arXiv:1502.05296 [hep-th].
- [7] E. Abdalla *et al.*, Cosmology Intertwined: A Review of the Particle Physics, Astrophysics, and Cosmology Associated with the Cosmological Tensions and Anomalies, in *2022 Snowmass Summer Study* (2022) arXiv:2203.06142 [astro-ph.CO].
- [8] E. Di Valentino *et al.*, Snowmass2021 - Letter of interest cosmology intertwined II: The hubble constant tension, *Astropart. Phys.* **131**, 102605 (2021), arXiv:2008.11284 [astro-ph.CO].
- [9] E. Di Valentino *et al.*, Cosmology intertwined III:  $f\sigma_8$  and  $S_8$ , *Astropart. Phys.* **131**, 102604 (2021), arXiv:2008.11285 [astro-ph.CO].
- [10] L. Heisenberg, H. Villarrubia-Rojo, and J. Zosso, Simultaneously solving the  $H_0$  and  $\sigma_8$  tensions with late dark energy, *Phys. Dark Univ.* **39**, 101163 (2023), arXiv:2201.11623 [astro-ph.CO].
- [11] A. G. Riess, The Expansion of the Universe is Faster than Expected, *Nature Rev. Phys.* **2**, 10 (2019), arXiv:2001.03624 [astro-ph.CO].
- [12] C. Heymans *et al.*, KiDS-1000 Cosmology: Multi-probe weak gravitational lensing and spectroscopic galaxy clustering constraints, *Astron. Astrophys.* **646**, A140 (2021), arXiv:2007.15632 [astro-ph.CO].
- [13] R. C. Nunes and S. Vagnozzi, Arbitrating the  $S_8$  discrepancy with growth rate measurements from redshift-space distortions, *Mon. Not. Roy. Astron. Soc.* **505**, 5427 (2021), arXiv:2106.01208 [astro-ph.CO].
- [14] L. Heisenberg, H. Villarrubia-Rojo, and J. Zosso, Can late-time extensions solve the  $H_0$  and  $\sigma_8$  tensions?, *Phys. Rev. D* **106**, 043503 (2022), arXiv:2202.01202 [astro-ph.CO].
- [15] E. Di Valentino, O. Mena, S. Pan, L. Visinelli, W. Yang, A. Melchiorri, D. F. Mota, A. G. Riess, and J. Silk, In the realm of the Hubble tension—a review of solutions, *Class. Quant. Grav.* **38**, 153001 (2021), arXiv:2103.01183 [astro-ph.CO].
- [16] T. Clifton, P. G. Ferreira, A. Padilla, and C. Skordis, Modified Gravity and Cosmology, *Phys. Rept.* **513**, 1 (2012), arXiv:1106.2476 [astro-ph.CO].
- [17] S. Nojiri and S. D. Odintsov, Introduction to modified gravity and gravitational alternative for dark energy, *eConf C0602061*, 06 (2006), arXiv:hep-th/0601213.
- [18] A. Einstein, Riemannian geometry with maintaining the notion of distant parallelism, *Sitz. Preuss. Akad. Wiss* **217** (1928).
- [19] A. Unzicker and T. Case, Translation of einstein’s attempt of a unified field theory with teleparallelism, arXiv:physics/0503046 (2005).
- [20] A. Einstein, A theory of gravitation, *Math. Ann.* **102**, 685 (1930).
- [21] A. Einstein, A theory of gravitation, *Sitzungsber. Preuss. Akad. Wiss. Phys. Math. Kl.* **401** (1930).
- [22] C. Pellegrini and J. Plebanski, A theory of gravitation, *Math.-Fys. Skr. Dan. Vid. Selskab* **2** (1962).
- [23] C. Møller, On the crisis in the theory of gravitation and a possible solution, *K. Dan. Vidensk. Selsk., Mat.-Fys. Medd* **39**, 1 (1978).
- [24] K. Hayashi and T. Nakano, Extended translation invariance and associated gauge fields, *Progress of Theoretical Physics* **38**, 491 (1967).
- [25] K. Hayashi and T. Shirafuji, New general relativity, *Phys. Rev. D* **19**, 3524 (1979).
- [26] J. G. Pereira, Teleparallelism: A New Insight Into Gravity, in *Handbook of Spacetime*, edited by A. Ashtekar and V. Petkov (Springer, 2014) pp. 197–212, 1302.6983 [gr-qc].
- [27] V. C. de Andrade, L. C. T. Guillen, and J. G. Pereira, Gravitational energy momentum density in teleparallel gravity, *Phys. Rev. Lett.* **84**, 4533 (2000), arXiv:gr-qc/0003100 [gr-qc].
- [28] H. I. Arcos and J. G. Pereira, Torsion gravity: A Reappraisal, *Int. J. Mod. Phys. D* **13**, 2193 (2004), arXiv:gr-qc/0501017 [gr-qc].
- [29] J. G. Pereira and Y. N. Obukhov, Gauge Structure of Teleparallel Gravity, *Proceedings, Teleparallel Universes in Salamanca: Salamanca, Spain, November 26-28, 2018*, *Universe* **5**, 139 (2019), arXiv:1906.06287 [gr-qc].
- [30] R. Aldrovandi and J. G. Pereira, *Teleparallel gravity: an introduction*, Vol. 173 (Springer Science & Business Media, 2012).
- [31] G. R. Bengochea and R. Ferraro, Dark torsion as the cosmic speed-up, *Phys. Rev.* **D79**, 124019 (2009), arXiv:0812.1205 [astro-ph].
- [32] E. V. Linder, Einstein’s Other Gravity and the Acceleration of the Universe, *Phys. Rev.* **D81**, 127301 (2010), arXiv:1005.3039 [astro-ph.CO].
- [33] B. Li, T. P. Sotiriou, and J. D. Barrow, Large-scale Structure in  $f(T)$  Gravity, *Phys. Rev. D* **83**, 104017 (2011), arXiv:1103.2786 [astro-ph.CO].
- [34] S.-F. Yan, P. Zhang, J.-W. Chen, X.-Z. Zhang, Y.-F. Cai, and E. N. Saridakis, Interpreting cosmological tensions from the effective field theory of torsional gravity, *Phys. Rev. D* **101**, 121301 (2020), arXiv:1909.06388 [astro-ph.CO].
- [35] M. Hohmann, L. Järv, and U. Ualikhanova, Covariant formulation of scalar-torsion gravity, *Phys. Rev. D* **97**, 104011 (2018), arXiv:1801.05786 [gr-qc].
- [36] M. Gonzalez-Espinoza and G. Otalora, Generating primordial fluctuations from modified teleparallel gravity with local Lorentz-symmetry breaking, *Phys. Lett. B* **809**, 135696 (2020), arXiv:2005.03753 [gr-qc].
- [37] K. K. Yerzhanov, S. R. Myrzakul, I. I. Kulnazarov, and R. Myrzakulov, Accelerating cosmology in  $F(T)$  gravity with scalar field, arXiv:1006.3879 (2010), arXiv:1006.3879 [gr-qc].
- [38] S. Chakrabarti, J. L. Said, and G. Farrugia, Some aspects of reconstruction using a scalar field in  $f(T)$  gravity, *Eur. Phys. J. C* **77**, 815 (2017), arXiv:1711.04423 [gr-qc].
- [39] K. Rezazadeh, A. Abdolmaleki, and K. Karami, Power-law and intermediate inflationary models in  $f(T)$ -gravity, *JHEP* **01**, 131, arXiv:1509.08769 [gr-qc].
- [40] P. Goodarzi and H. Mohseni Sadjadi, Reheating in a modified teleparallel model of inflation, *Eur. Phys. J. C*

- 79**, 193 (2019), arXiv:1808.01225 [physics.gen-ph].
- [41] K. Bamba, G. G. L. Nashed, W. El Hanafy, and S. K. Ibraheem, Bounce inflation in  $f(T)$  Cosmology: A unified inflaton-quintessence field, *Phys. Rev. D* **94**, 083513 (2016), arXiv:1604.07604 [gr-qc].
- [42] C.-Q. Geng, C.-C. Lee, E. N. Saridakis, and Y.-P. Wu, Teleparallel dark energy, *Phys. Lett. B* **704**, 384 (2011), arXiv:1109.1092 [hep-th].
- [43] C.-Q. Geng, C.-C. Lee, and E. N. Saridakis, Observational Constraints on Teleparallel Dark Energy, *JCAP* **1201**, 002, arXiv:1110.0913 [astro-ph.CO].
- [44] C. Xu, E. N. Saridakis, and G. Leon, Phase-Space analysis of Teleparallel Dark Energy, *JCAP* **1207**, 005, arXiv:1202.3781 [gr-qc].
- [45] H. Wei, Dynamics of Teleparallel Dark Energy, *Phys. Lett. B* **712**, 430 (2012), arXiv:1109.6107 [gr-qc].
- [46] G. Otalora, Scaling attractors in interacting teleparallel dark energy, *JCAP* **1307**, 044, arXiv:1305.0474 [gr-qc].
- [47] G. Otalora, Cosmological dynamics of tachyonic teleparallel dark energy, *Phys. Rev. D* **88**, 063505 (2013), arXiv:1305.5896 [gr-qc].
- [48] G. Otalora, A novel teleparallel dark energy model, *Int. J. Mod. Phys. D* **25**, 1650025 (2015), arXiv:1402.2256 [gr-qc].
- [49] M. A. Skugoreva, E. N. Saridakis, and A. V. Toporensky, Dynamical features of scalar-torsion theories, *Phys. Rev. D* **91**, 044023 (2015), arXiv:1412.1502 [gr-qc].
- [50] L. Jarv and A. Toporensky, General relativity as an attractor for scalar-torsion cosmology, *Phys. Rev. D* **93**, 024051 (2016), arXiv:1511.03933 [gr-qc].
- [51] M. Gonzalez-Espinoza, G. Otalora, N. Videla, and J. Saavedra, Slow-roll inflation in generalized scalar-torsion gravity, *JCAP* **08**, 029, arXiv:1904.08068 [gr-qc].
- [52] M. Gonzalez-Espinoza and G. Otalora, Cosmological dynamics of dark energy in scalar-torsion  $f(T, \phi)$  gravity, *Eur. Phys. J. C* **81**, 480 (2021), arXiv:2011.08377 [gr-qc].
- [53] M. Gonzalez-Espinoza, R. Herrera, G. Otalora, and J. Saavedra, Reconstructing inflation in scalar-torsion  $f(T, \phi)$  gravity, *Eur. Phys. J. C* **81**, 731 (2021), arXiv:2106.06145 [gr-qc].
- [54] M. Gonzalez-Espinoza, G. Otalora, and J. Saavedra, Stability of scalar perturbations in scalar-torsion  $f(T, \phi)$  gravity theories in the presence of a matter fluid, *JCAP* **10**, 007, arXiv:2101.09123 [gr-qc].
- [55] V. Faraoni, *Cosmology in scalar tensor gravity*, Vol. 139 (2004).
- [56] A. D. Linde, Coleman-Weinberg Theory and a New Inflationary Universe Scenario, *Phys. Lett. B* **114**, 431 (1982).
- [57] D. Z. Freedman, I. J. Muzinich, and E. J. Weinberg, On the Energy-Momentum Tensor in Gauge Field Theories, *Annals Phys.* **87**, 95 (1974).
- [58] D. Z. Freedman and E. J. Weinberg, The Energy-Momentum Tensor in Scalar and Gauge Field Theories, *Annals Phys.* **87**, 354 (1974).
- [59] N. D. Birrell and P. C. W. Davies, *Quantum Fields in Curved Space* (Cambridge Univ. Press, Cambridge, UK, 1984).
- [60] G. Leon, A. Paliathanasis, E. N. Saridakis, and S. Basilakos, Unified dark sectors in scalar-torsion theories of gravity, *Phys. Rev. D* **106**, 024055 (2022), arXiv:2203.14866 [gr-qc].
- [61] L. K. Duchaniya, S. A. Kadam, J. Levi Said, and B. Mishra, Dynamical systems analysis in  $f(T, \phi)$  gravity, (2022), arXiv:2209.03414 [gr-qc].
- [62] L. K. Duchaniya, B. Mishra, and J. Levi Said, Noether Symmetry Approach in Scalar-Torsion  $f(T, \phi)$  Gravity, (2022), arXiv:2210.11944 [gr-qc].
- [63] Y. Leyva, C. Leiva, G. Otalora, and J. Saavedra, Inflation and primordial fluctuations in  $F(T)$  gravity's rainbow, *Phys. Rev. D* **105**, 043523 (2022), arXiv:2111.07098 [gr-qc].
- [64] Y.-F. Cai, S. Capozziello, M. De Laurentis, and E. N. Saridakis,  $f(T)$  teleparallel gravity and cosmology, *Rept. Prog. Phys.* **79**, 106901 (2016), arXiv:1511.07586 [gr-qc].
- [65] A. De Felice, L. Heisenberg, R. Kase, S. Mukohyama, S. Tsujikawa, and Y.-l. Zhang, Cosmology in generalized Proca theories, *JCAP* **06**, 048, arXiv:1603.05806 [gr-qc].
- [66] A. De Felice, L. Heisenberg, R. Kase, S. Mukohyama, S. Tsujikawa, and Y.-l. Zhang, Effective gravitational couplings for cosmological perturbations in generalized Proca theories, *Phys. Rev. D* **94**, 044024 (2016), arXiv:1605.05066 [gr-qc].
- [67] S. Nakamura, R. Kase, and S. Tsujikawa, Coupled vector dark energy, *JCAP* **12**, 032, arXiv:1907.12216 [gr-qc].
- [68] A. De Felice, S. Nakamura, and S. Tsujikawa, Suppressed cosmic growth in coupled vector-tensor theories, *Phys. Rev. D* **102**, 063531 (2020), arXiv:2004.09384 [gr-qc].
- [69] T. Koivisto and D. F. Mota, Vector Field Models of Inflation and Dark Energy, *JCAP* **08**, 021, arXiv:0805.4229 [astro-ph].
- [70] L. H. Ford, INFLATION DRIVEN BY A VECTOR FIELD, *Phys. Rev. D* **40**, 967 (1989).
- [71] A. B. Burd and J. E. Lidsey, An Analysis of inflationary models driven by vector fields, *Nucl. Phys. B* **351**, 679 (1991).
- [72] C. Armendariz-Picon, Could dark energy be vector-like?, *JCAP* **07**, 007, arXiv:astro-ph/0405267.
- [73] L. G. Gomez and Y. Rodriguez, Coupled multi-Proca vector dark energy, *Phys. Dark Univ.* **31**, 100759 (2021), arXiv:2004.06466 [gr-qc].
- [74] A. Golovnev, V. Mukhanov, and V. Vanchurin, Vector Inflation, *JCAP* **06**, 009, arXiv:0802.2068 [astro-ph].
- [75] M. Gonzalez-Espinoza, G. Otalora, J. Saavedra, and N. Videla, Growth of matter overdensities in non-minimal torsion-matter coupling theories, *Eur. Phys. J. C* **78**, 799 (2018), arXiv:1808.01941 [gr-qc].
- [76] E. J. Copeland, M. Sami, and S. Tsujikawa, Dynamics of dark energy, *Int. J. Mod. Phys. D* **15**, 1753 (2006), arXiv:hep-th/0603057.
- [77] L. Amendola and S. Tsujikawa, *Dark energy: theory and observations* (Cambridge University Press, 2010).
- [78] L. Amendola, Scaling solutions in general nonminimal coupling theories, *Phys. Rev. D* **60**, 043501 (1999), arXiv:astro-ph/9904120.
- [79] P. G. Ferreira and M. Joyce, Cosmology with a primordial scaling field, *Phys. Rev. D* **58**, 023503 (1998), arXiv:astro-ph/9711102.
- [80] R. Bean, S. H. Hansen, and A. Melchiorri, Early universe constraints on a primordial scaling field, *Phys. Rev. D* **64**, 103508 (2001), arXiv:astro-ph/0104162.
- [81] Y. Akrami *et al.* (Planck), Planck 2018 results. X. Constraints on inflation, arXiv:1807.06211 [astro-ph] (2018), 1807.06211 [astro-ph.CO].

- [82] N. Aghanim *et al.* (Planck), Planck 2018 results. VI. Cosmological parameters, *Astron. Astrophys.* **641**, A6 (2020), arXiv:1807.06209 [astro-ph.CO].
- [83] P. Ade *et al.* (Planck), Planck 2015 results. XIV. Dark energy and modified gravity, *Astron. Astrophys.* **594**, A14 (2016), arXiv:1502.01590 [astro-ph.CO].
- [84] O. Farooq, F. R. Madiyar, S. Crandall, and B. Ratra, Hubble Parameter Measurement Constraints on the Redshift of the Deceleration–acceleration Transition, Dynamical Dark Energy, and Space Curvature, *Astrophys. J.* **835**, 26 (2017), arXiv:1607.03537 [astro-ph.CO].
- [85] J. Ryan, S. Doshi, and B. Ratra, Constraints on dark energy dynamics and spatial curvature from Hubble parameter and baryon acoustic oscillation data, *Mon. Not. Roy. Astron. Soc.* **480**, 759 (2018), arXiv:1805.06408 [astro-ph.CO].
- [86] I. S. Albuquerque, N. Frusciante, N. J. Nunes, and S. Tsujikawa, New scaling solutions in cubic Horndeski theories, *Phys. Rev. D* **98**, 064038 (2018), arXiv:1807.09800 [gr-qc].
- [87] J. Ohashi and S. Tsujikawa, Assisted dark energy, *Phys. Rev. D* **80**, 103513 (2009), arXiv:0909.3924 [gr-qc].
- [88] V. Mukhanov, *Physical foundations of cosmology* (Cambridge University Press, 2005).
- [89] L. Amendola, Coupled quintessence, *Phys. Rev. D* **62**, 043511 (2000), arXiv:astro-ph/9908023.
- [90] L. Amendola, Perturbations in a coupled scalar field cosmology, *Mon. Not. Roy. Astron. Soc.* **312**, 521 (2000), arXiv:astro-ph/9906073.
- [91] Z. Davari, V. Marra, and M. Malekjani, Cosmological constraints on minimally and non-minimally coupled scalar field models, *Mon. Not. Roy. Astron. Soc.* **491**, 1920 (2020), arXiv:1911.00209 [gr-qc].
- [92] C. Zhang, H. Zhang, S. Yuan, S. Liu, T.-J. Zhang, and Y.-C. Sun, Four new observational  $h(z)$  data from luminous red galaxies in the sloan digital sky survey data release seven, *Res. Astron. Astrophys.* **14**, 1221 (2014).
- [93] J. Simon, L. Verde, and R. Jimenez, Constraints on the redshift dependence of the dark energy potential, *Phys. Rev. D* **71**, 123001 (2005).
- [94] M. Moresco, A. Cimatti, R. Jimenez, L. Pozzetti, G. Zamorani, M. Bolzonella, J. Dunlop, F. Lamareille, M. Mignoli, H. Pearce, *et al.*, Improved constraints on the expansion rate of the universe up to  $z \sim 1.1$  from the spectroscopic evolution of cosmic chronometers, *J. Cosmol. Astropart. Phys.* **2012** (08), 006.
- [95] A. J. Cuesta, M. Vargas-Magaña, F. Beutler, A. S. Bolton, J. R. Brownstein, D. J. Eisenstein, H. Gil-Marín, S. Ho, C. K. McBride, C. Maraston, *et al.*, The clustering of galaxies in the sdss-iii baryon oscillation spectroscopic survey: Baryon acoustic oscillations in the correlation function of low- $z$  and cmass galaxies in data release 12, *Mon. Not. R. Astron. Soc.* **457**, 1770 (2016).
- [96] C. Blake, S. Brough, M. Colless, C. Contreras, W. Couch, S. Croom, D. Croton, T. M. Davis, M. J. Drinkwater, K. Forster, *et al.*, The wigglez dark energy survey: Joint measurements of the expansion and growth history at  $z \lesssim 1$ , *Mon. Not. R. Astron. Soc.* **425**, 405 (2012).
- [97] A. Ratsimbazafy, S. Loubser, S. Crawford, C. Cress, B. Bassett, R. Nichol, and P. Väisänen, Age-dating luminous red galaxies observed with the southern african large telescope, *Mon. Not. R. Astron. Soc.* **467**, 3239 (2017).
- [98] D. Stern, R. Jimenez, L. Verde, M. Kamionkowski, and S. A. Stanford, Cosmic chronometers: constraining the equation of state of dark energy. i:  $H(z)$  measurements, *J. Cosmol. Astropart. Phys.* **2010** (02), 008.
- [99] M. Moresco, Raising the bar: new constraints on the hubble parameter with cosmic chronometers at  $z \sim 2$ , *Mon. Not. R. Astron. Soc.* **450**, L16 (2015).
- [100] T. Delubac, J. E. Bautista, J. Rich, D. Kirkby, S. Bailey, A. Font-Ribera, A. Slosar, K.-G. Lee, M. M. Pieri, J.-C. Hamilton, *et al.*, Baryon acoustic oscillations in the lyc forest of boss dr11 quasars, *A&A* **574**, 59 (2015).
- [101] A. Font-Ribera, D. Kirkby, J. Miralda-Escudé, N. P. Ross, A. Slosar, J. Rich, É. Aubourg, S. Bailey, V. Bhardwaj, J. Bautista, *et al.*, Quasar-lyman  $\alpha$  forest cross-correlation from boss dr11: Baryon acoustic oscillations, *J. Cosmol. Astropart. Phys.* **2014** (05), 027.

### Appendix A: Eigenvalues of points f and g

Point  $f$  has the eigenvalues

$$\begin{aligned}
\mu_1 &= 0, & \mu_2 &= -2, & \mu_3 &= -3, \\
\mu_4 &= \frac{1}{2} \left( -\sqrt{24\lambda_2 y_{2c}^2 + 1} - 3 \right), \\
\mu_5 &= \frac{1}{2} \left( \sqrt{24\lambda_2 y_{2c}^2 + 1} - 3 \right), \\
\mu_6 &= \frac{-\sqrt{3}\sqrt{A} - 9\lambda_1 y_{2c}^2 - 3\sigma_1}{2(3\lambda_1 y_{2c}^2 + \sigma_1)} \\
\mu_7 &= \frac{\sqrt{3}\sqrt{A} - 9\lambda_1 y_{2c}^2 - 3\sigma_1}{2(3\lambda_1 y_{2c}^2 + \sigma_1)}, \tag{A1}
\end{aligned}$$

where,

$$\begin{aligned}
A &= 108\lambda_1^3 \sigma_1 y_{2c}^6 - 36\lambda_1^3 \sigma_1 y_{2c}^4 - 12\lambda_1 \sigma_1^3 y_{2c}^2 + 18\lambda_1 \sigma_1 y_{2c}^2 \\
&+ 27\lambda_1^2 y_{2c}^4 + 4\lambda_1 \sigma_1^3 + 3\sigma_1^2.
\end{aligned}$$

Point  $g$  has the eigenvalues

$$\begin{aligned}
\mu_1 &= 0, & \mu_2 &= -2, & \mu_3 &= -3, \\
\mu_4 &= \frac{1}{2} \left( -\sqrt{\frac{A - 6\sqrt{B}}{\lambda_2(3\lambda_1 \lambda_2 x_{3c}^2 + \lambda_2 \sigma_1 + \lambda_1)}} - 3 \right), \\
\mu_5 &= \frac{1}{2} \left( \sqrt{\frac{A - 6\sqrt{B}}{\lambda_2(3\lambda_1 \lambda_2 x_{3c}^2 + \lambda_2 \sigma_1 + \lambda_1)}} - 3 \right), \\
\mu_6 &= \frac{1}{2} \left( -\sqrt{\frac{A + 6\sqrt{B}}{\lambda_2(3\lambda_1 \lambda_2 x_{3c}^2 + \lambda_2 \sigma_1 + \lambda_1)}} - 3 \right), \\
\mu_7 &= \frac{1}{2} \left( \sqrt{\frac{A + 6\sqrt{B}}{\lambda_2(3\lambda_1 \lambda_2 x_{3c}^2 + \lambda_2 \sigma_1 + \lambda_1)}} - 3 \right), \tag{A2}
\end{aligned}$$

where,

$$\begin{aligned}
A &= 6\lambda_1^2 \sigma_1 (3\lambda_2 x_{3c}^2 + 1) (\lambda_2 (3x_{3c}^2 - 1) + 1) \\
&+ 3\lambda_2 \lambda_1 (2\sigma_1^2 (-3\lambda_2 x_{3c}^2 + \lambda_2 - 1) + \lambda_2 x_{3c}^2 + 3) \\
&+ 3\lambda_2^2 \sigma_1 (8x_{3c}^2 (\lambda_2 (6x_{3c}^2 - 2) + 1) + 3),
\end{aligned}$$

and,

$$\begin{aligned}
B &= 16\lambda_1 \lambda_2^2 \sigma_1 x_{3c}^2 (\lambda_2 (3x_{3c}^2 - 1) + 1) (3\lambda_1 \lambda_2 x_{3c}^2 + \lambda_2 \sigma_1 + \lambda_1) \\
&(\lambda_2 \sigma_1 (6x_{3c}^2 - 2) + \lambda_1 + \sigma_1) + (3\lambda_2^2 (3\lambda_1^2 + 8\lambda_2) \sigma_1 x_{3c}^4 \\
&- \lambda_2 x_{3c}^2 (3(\lambda_2 - 2)\lambda_1^2 \sigma_1 + \lambda_2 \lambda_1 (3\sigma_1^2 + 4) + 4\lambda_2 (2\lambda_2 - 1)\sigma_1) \\
&+ \lambda_1 (\lambda_2 - 1)\sigma_1 (\lambda_2 \sigma_1 - \lambda_1))^2.
\end{aligned}$$

### Appendix B: Hubble's parameter data

Within this appendix, we provide the dataset comprising Hubble's parameter values for the redshift range of  $0.01 < z < 2.360$ :

TABLE III. Hubble's parameter vs. redshift & scale factor.

$z$	$H(z)$ ( $\frac{km/s}{Mpc}$ )	Ref.
0.07	$69 \pm 19.6$	[92]
0.09	$69 \pm 12$	[93]
0.100	$69 \pm 12$	[93]
0.120	$68.6 \pm 26.2$	[92]
0.170	$83 \pm 8$	[93]
0.179	$75 \pm 4$	[94]
0.199	$75 \pm 5$	[94]
0.200	$72.9 \pm 29.6$	[92]
0.270	$77 \pm 14$	[93]
0.280	$88.8 \pm 36.6$	[92]
0.320	$79.2 \pm 5.6$	[95]
0.352	$83 \pm 14$	[94]
0.3802	$83 \pm 13.5$	[94]
0.400	$95 \pm 17$	[93]
0.4004	$77 \pm 10.2$	[94]
0.4247	$87.1 \pm 11.2$	[94]
0.440	$82.6 \pm 7.8$	[96]
0.4497	$92.8 \pm 12.9$	[94]
0.470	$89 \pm 50$	[97]
0.4783	$80.9 \pm 9$	[94]
0.480	$97 \pm 62$	[98]
0.570	$100.3 \pm 3.7$	[95]
0.593	$104 \pm 13$	[94]
0.600	$87.9 \pm 6.1$	[96]
0.680	$92 \pm 8$	[94]
0.730	$97.3 \pm 7$	[96]
0.781	$105 \pm 12$	[94]
0.875	$125 \pm 17$	[94]
0.880	$90 \pm 40$	[98]
0.900	$117 \pm 23$	[93]
1.037	$154 \pm 20$	[94]
1.300	$168 \pm 17$	[93]
1.363	$160 \pm 33.6$	[99]
1.430	$177 \pm 18$	[93]
1.530	$140 \pm 14$	[93]
1.750	$202 \pm 40$	[93]
1.965	$186.5 \pm 50.4$	[99]
2.340	$222 \pm 7$	[100]
2.360	$226 \pm 8$	[101]